ELSEVIER

Chemical Engineering Journal 140 (2008) 614–620

Chemical Engineering Journal

www.elsevier.com/locate/cej

Short communication

Diffusion of hydrocarbon mixtures in MFI zeolite: Influence of intersection blocking

R. Krishna*, J.M. van Baten

Van't Hoff Institute for Molecular Sciences, University of Amsterdam, Nieuwe Achtergracht 166, 1018 WV Amsterdam, The Netherlands

Received 30 October 2007; received in revised form 17 November 2007; accepted 19 November 2007

Abstract

Branched and cyclic hydrocarbons such as *iso*-butane, 2-methylpentane, 3-methylpentane, 2,2-dimethyl-butane and benzene are preferentially adsorbed at the intersections of the channels of MFI zeolite; they serve as bottlenecks for molecular traffic in mixtures with linear C1–C6 alkanes. Molecular dynamics simulations show that as the loadings of tardier *i*C4, 2MP, 3MP, 22DMB, and Bz is progressively increased to four molecules per unit cell the diffusivity of the more mobile linear alkane reduces nearly to zero. The reduction in the *n*-alkane diffusivity is quantitatively similar irrespective of the branched/cyclic hydrocarbon.

Keywords: MFI zeolite; Self-diffusivity; Hydrocarbon mixtures; Branched hydrocarbons; Cyclic hydrocarbons; Molecular dynamics; Adsorption

1. Introduction

MFI zeolite membranes offer considerable potential for separating hydrocarbon mixtures [1–8]. The separation selectivity is dictated both by the adsorption and diffusion characteristics of the individual species in the mixture. In MFI zeolite each component in the mixture is influenced by the co-adsorbed species [9]; almost invariably the more mobile species is slowed down due to the presence of tardier partners. PFG NMR studies of Förste et al. [10] found that the self-diffusivity of methane (C1), D_{C1}, is significantly reduced as the loading of the co-adsorbed benzene (Bz), q_{Bz}, increases. In MAS PFG NMR studies, Fernandez et al. [11] found that the self-diffusivity of *n*-butane (*n*C4), D_{nC4}, in mixtures with *iso*-butane (*i*C4) decreases by an order of magnitude as the loading of *i*C4, q_{iC4}, is increased from 0 to 2 molecules per unit cell. For *n*-hexane (*n*C6)–2-methylpentane (2MP), and *n*C6–3-methylpentane (3MP) mixtures experimental studies [12,13] show that the D_{nC6} is reduced significantly as the 2MP or 3MP loadings increase.

The major aim of the present communication is to demonstrate that the observed reduction in the diffusivity of the linear alkane in C1–Bz, *n*C4–*i*C4, and *n*C6–2MP mixtures is characteristic of a much wider variety of mixtures. We aim to show that the tardier branched or cyclic hydrocarbons reduce molecular traffic along the channels of MFI by blocking the intersections where they prefer to locate. Using molecular dynamics (MD), we determined the self-diffusivity of a linear C1–C6 alkane in a wide variety of mixtures: C1–*i*C4, ethane (C2)–iC4, propane (C3)–iC4, *n*C4–*i*C4, *n*C6–2MP, *n*C6–3MP, *n*C6–2,2-dimethylbutane (22DMB), *n*C6–Bz, C1–22DMB, C1–Bz, and C3–Bz. Besides MD simulations we performed Configurational-Bias Monte-Carlo (CBMC) simulations to determine the adsorption equilibrium for pure components and binary mixtures. The CBMC and MD simulation methodologies are described in Supplementary Information accompanying this publication, along with pure component, and mixture adsorption data, snapshots and detailed simulation results for diffusivities. A selection of these results is discussed below.

2. Simulations of adsorption

CBMC simulations of the adsorption isotherms for C1, C2, C3, *n*C4, *i*C4, *n*C6, 2MP, 3MP, 22DMB, and Bz in MFI at 300 K are shown in Fig. 1a–c. We note that branched and cyclic hydrocarbons such as *i*C4, 2MP, 3MP, and Bz show a strong inflection at a loading, $q = 4$ molecules per unit cell. These molecules prefer to locate at the intersections because of the extra "leg room"

* Corresponding author. Tel.: +31 20 5257007; fax: +31 20 5255604.
E-mail address: r.krishna@uva.nl (R. Krishna).

1385-8947/$ – see front matter © 2007 Elsevier B.V. All rights reserved.
doi:10.1016/j.cej.2007.11.026

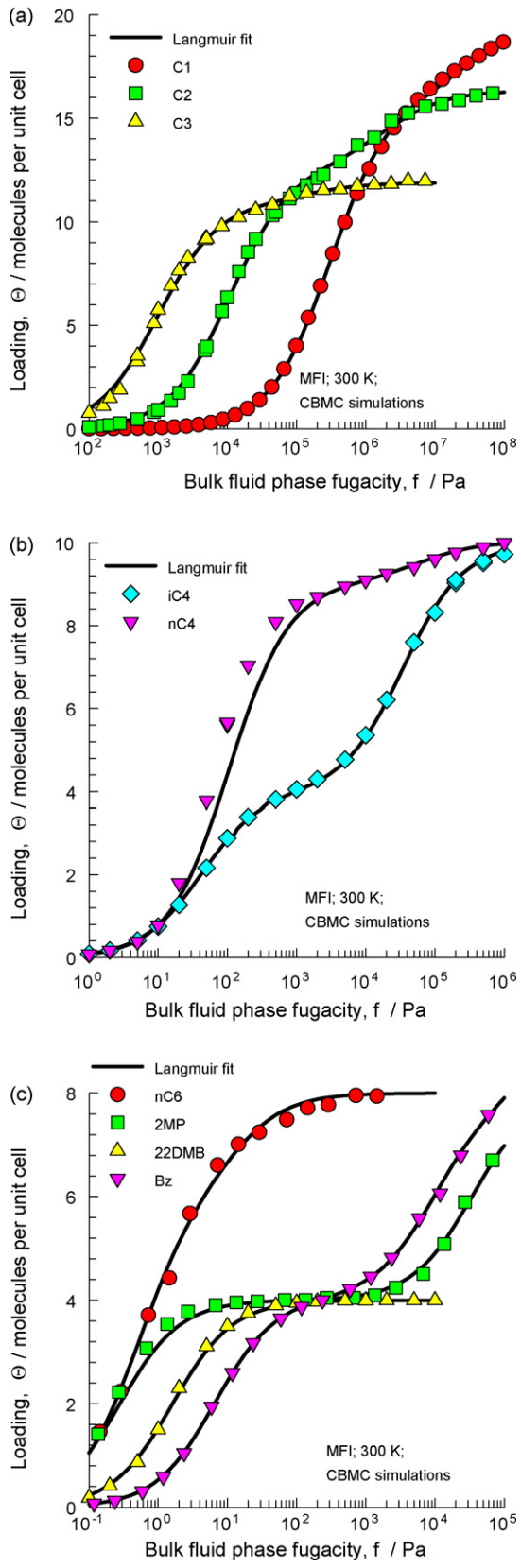

Fig. 1. CBMC simulations for pure component isotherms in MFI at 300 K for (a) C1, C2, C3, (b) *n*C4, *i*C4, (c) *n*C6, 2MP, 3MP, 22DMB, and Bz. The continuous solid lines represent 3-site Langmuir fits; the parameter values are given in Supplementary Information.

that is available here. An extra "push" is required to locate these molecules within the channel interiors; this extra push results in an inflection in the pure component isotherms at a loading of four molecules per unit cell [14–17]. For the compact and bulky 22DMB, the extra push is too large, and therefore $q = 4$ is also the saturation capacity.

The preferential location of *i*C4, 2MP, 3MP, 22DMB, and Bz at intersections also manifests for mixture adsorption, as illustrated in the snapshots in Fig. 2 for C3–*i*C4, C1–Bz, and *n*C6–22DMB mixtures. We see that *i*C4, Bz and 2MP are exclusively located at the intersections. The isotherm inflection has a significant influence on mixture adsorption, as illustrated for (a) *n*C4–*i*C4, (b) *n*C6–Bz, and (c) *n*C6–2MP mixtures in Fig. 3. The component loadings of *i*C4, Bz and 2MP all exhibit a maximum when the total mixture loading $q = 4$. For $q > 4$, the adsorption of the linear alkane is favored because it is more efficient to pack the channels of MFI with *linear* alkanes. The separation of hexane isomers by exploiting the differences in the packing efficiency of molecules has been stressed in earlier publications [16,18,19]; the same principle applies to other hydrocarbon mixtures. For all the mixtures investigated in this study, the multicomponent Langmuir model cannot be used to estimate the component loadings in the mixture because this model is unable to predict the maximum in the loading of the branched or cyclic hydrocarbon in the mixture. The Ideal Adsorbed Solution Theory (IAST) of Myers and Prausnitz [20], using only pure component isotherm data, is successful in providing a good *qualitative* representation of entropy effects during mixture sorption [21]. The IAST predictions are shown by the continuous solid lines in Fig. 3a–c. As can be seen from Fig. 3 the *quantitative* agreement between the predictions of IAST and CBMC mixture simulations are not perfect for the branched or cyclic hydrocarbon. This failure of the IAST to provide a good quantitative description of mixture adsorption has also been stressed earlier for C1–Bz, and C1–cyclohexane (CH) mixtures by Murthi and Snurr [22]. The reason for this imperfect prediction is to be found in *segregation* effects in mixture adsorption [22,23] found in a variety of zeolites.

For mixture loadings $q > 4$, the adsorption becomes increasingly segregated; the intersections sites will be occupied by the branched or cyclic hydrocarbons while the channels, straight and zig–zag, will have to accommodate increasing amount of the linear alkanes. The IAST assumes a homogenous adsorbed phase composition, and therefore its predictions of *i*C4, Bz and 2MP loadings will become increasingly poor for $q > 4$. For a good quantitative description of mixture adsorption, non-ideality effects caused by segregation have to be taken account of using the Real Adsorbed Solution Theory [24].

3. Simulations of diffusion

We carried out a set of simulations to determine the self-diffusivities a linear C1–C6 alkane in a variety of binary mixtures in which the loading of the branched or cyclic hydrocarbon was varied in the range 0–4 molecules per unit cell. The self-diffusivities of the branched or cyclic hydrocarbons are not reported because these molecules did not move sufficiently long

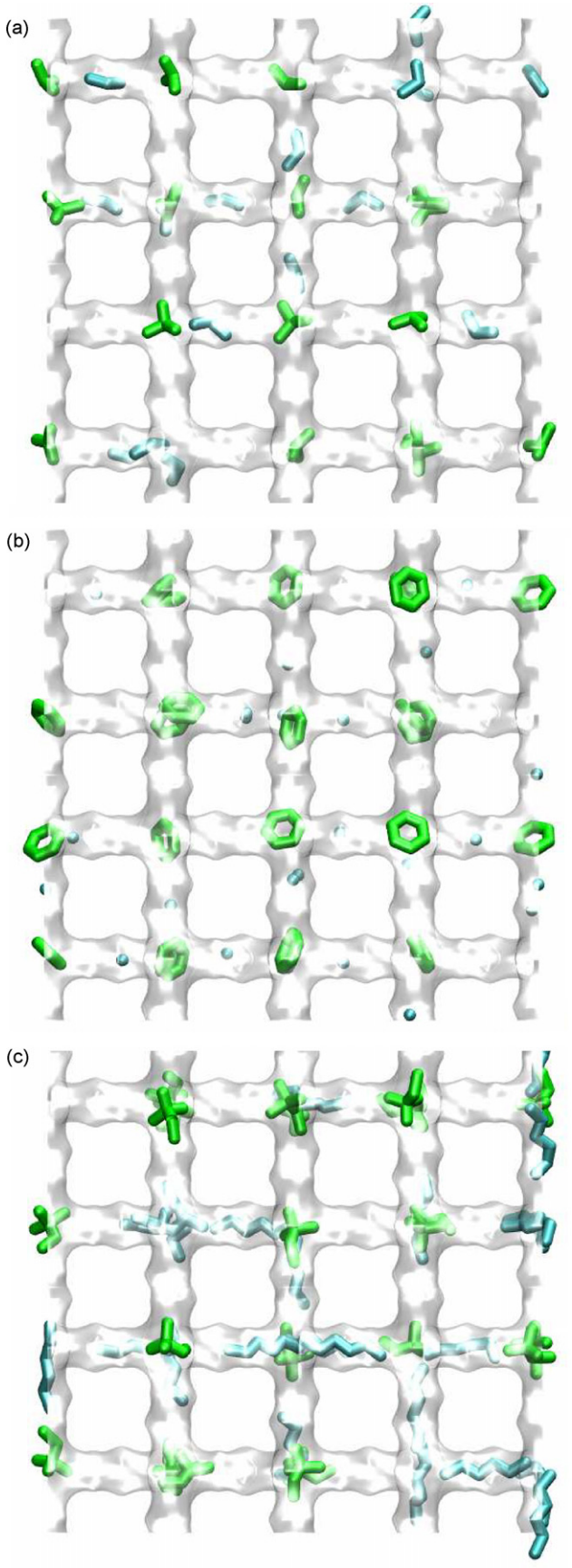

Fig. 2. Snapshots showing the location of (a) C3 and *i*C4, (b) C1 and Bz, and (c) *n*C6 and 22DMB, molecules in MFI, viewed from the side, in the *x*–*y* plane. The total loading $q = 4$, with equal loading of each species.

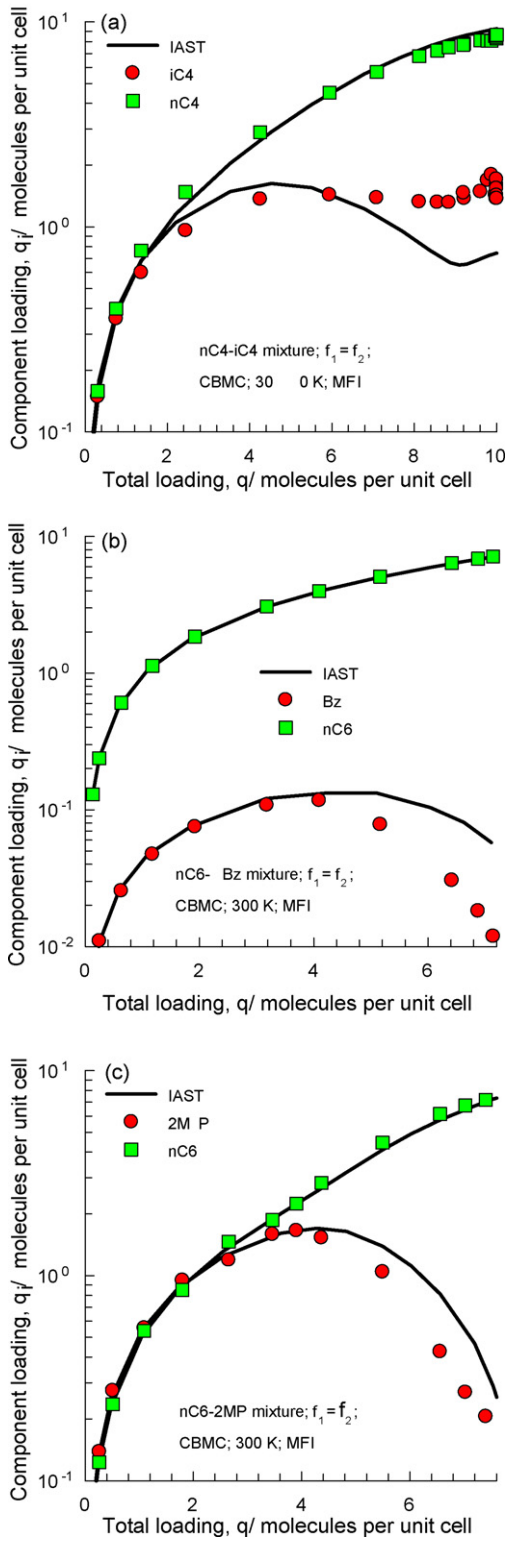

Fig. 3. CBMC simulations of the component loadings in (a) *n*C4–*i*C4, (b) *n*C6–Bz, and (c) *n*C6–2MP mixtures compared with the calculations of IAST, shown by the continuous solid lines.

distances during the simulation time in order to obtain reliable statistics required to calculate diffusivities.

Consider first diffusion in a mixture C1 and *i*C4 for which the total loading is maintained constant at $q = 4$. The self-diffusivity of C1 in *x*, *y*, and *z* directions of MFI are shown in Fig. 4a. The most prominent contribution is along the straight channels, in the *y*-direction. We note that $D_{C1,y}$ decreases practically linearly as q_{iC4} increases in value from 0 to 2. Fig. 4b and c present snapshots showing the location of C1 and *i*C4 for $q_{C1} = q_{iC4} = 2$; at this loading half the intersection sites are occupied by the extremely tardy *i*C4. Since the occupancy of the intersections is distributed randomly, each one of the straight channels has an *i*C4 molecule ensconced somewhere along the *y*-direction; see Fig. 4b and c. The occupation of *i*C4 at the intersections of the channels is tantamount to blockage, leading to severe reduction in the molecular traffic of the more mobile C1 along the straight channels. This explains the severe reduction in $D_{C1,y}$ at $q_{iC4} = 2$. For $q_{iC4} > 2$ the C1 molecules have to worm their way along the zig–zag channels in *x*- and *z*-directions, by-passing the blocked intersections. From Fig. 4a we note that for $q_{iC4} > 2$, $D_{C1,x} \approx D_{C1,y}$. An analogous picture emerges for each of the eleven binary mixtures investigated in the present study.

The orientation averaged diffusivity values for linear alkanes, $D = (D_x + D_y + D_z)/3$, are summarized in Fig. 5 as a function of the loading of its partner in various mixtures. From Fig. 5a we note that the dependence of D_{C1} on the loading of its partner, in mixtures with a constant total loading $q = 4$, is the same irrespective of its partner *i*C4, 22DMB, or Bz. We conclude that the blockage of the intersections by any one of *i*C4, 22DMB or Bz is *equally* deleterious to C1 traffic. The choice of total loading $q = 4$ in Fig. 5a is for illustration purposes; analogous results are obtained for $q > 4$.

Simulation results in which the loading of C1 in C1–Bz mixtures was maintained at $q_{C1} = 3$ are presented in Fig. 5b. The MD simulations are in excellent agreement with the results of Gupta and Snurr [25] who performed free energy perturbation calculations to determine D_{C1} in both C1–Bz and C1–CH mixtures; CH is ensconced at the intersections and reduces the traffic of C1 in same quantitative manner as *i*C4, 22DMB and Bz. The PFG NMR experiments of Förste et al. [10] for C1–Bz mixtures in ZSM-5 are also plotted in Fig. 5b for comparison; there is a good qualitative agreement between simulations and experiment.

The influence of increasing loading of *i*C4 on diffusion in C2–*i*C4 and *n*C4–*i*C4 mixtures is shown in Fig. 5c. The reduction of D_{C2} and D_{nC4} with q_{iC4} is similar; if the data were normalized with respect to pure linear alkane diffusivity, the results would fall on the same line. All normal alkanes experience a similar deleterious influence due to intersection blocking. Also plotted in Fig. 5c are the PFG NMR data of Fernandez et al. [11] for *n*C4–*i*C4 mixtures. The experiments show a sharp decline in D_{nC4} to virtually zero as q_{iC4} approaches 2; this decline is sharper than anticipated by MD simulations. The lack of perfect agreement between the MD simulations results for *n*C4–*i*C4 mixtures when compared to experimental data is due to the extreme sensitivity of MD simulations to very small alterations in the chosen force field [26].

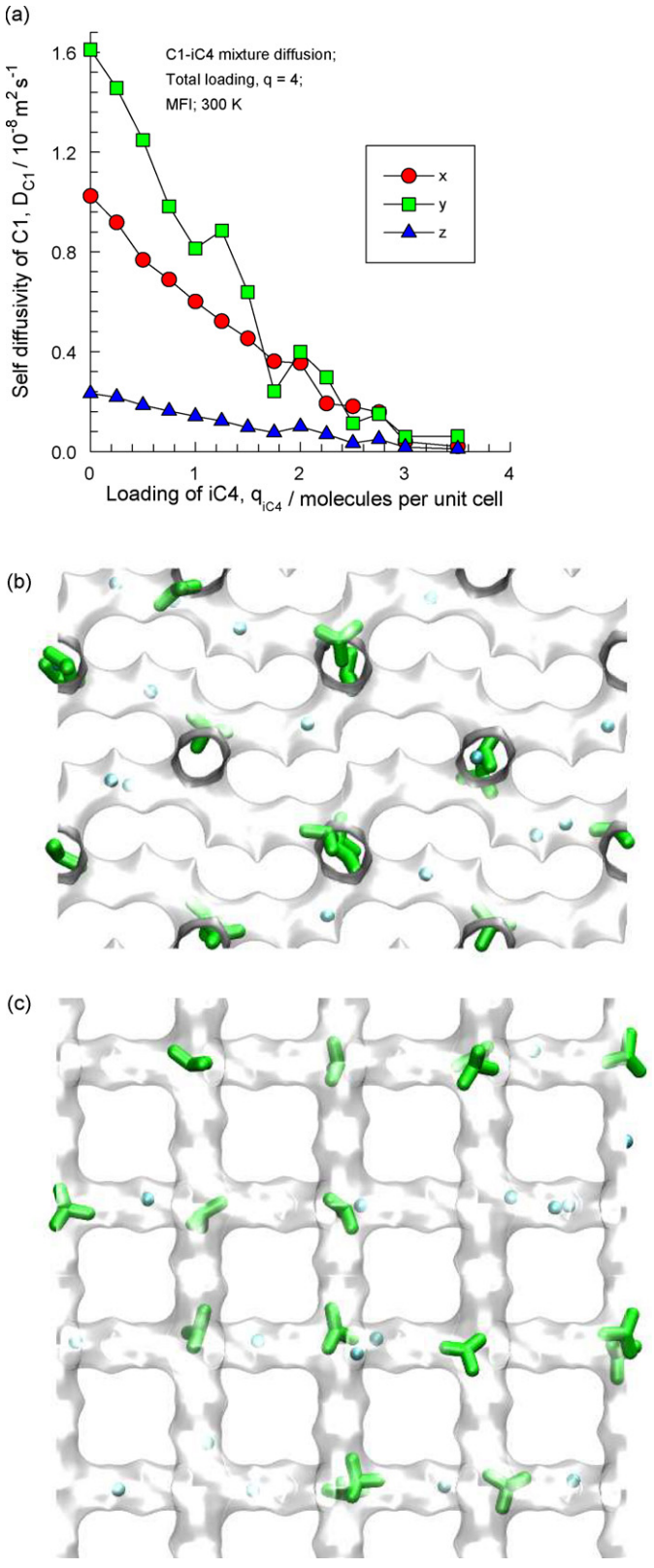

Fig. 4. (a) Self-diffusion coefficients of C1 in C1/*i*C4 mixtures in MFI at 300 K as a function of the loading of *i*C4 in the mixture. Snapshots showing the location of C1 and *i*C4 molecules in MFI, viewed (b) from the top, in the *x*–*z* plane, and (c) from the side, in the *x*–*y* plane. Both views are two unit cells deep. The total loading in the snapshot is $q = 4$, with equal loading of each species.

In MFI zeolite, any tardy species will slow down the diffusion of a more mobile species, and we can ask ourselves the question: what is peculiar about intersection blocking? To answer this question, we have included data for D_{C1} in C1–*n*C4, and C1–*n*C6 mixtures in Fig. 5a. *n*C4 and *n*C6 can adsorb anywhere in the MFI pore space and the reduction of D_{C1} is due to correlation effects [9]; the tardier partner (*n*C6) causes a greater reduction in D_{C1} than *n*C4. The influence of intersection blockage in C1–*i*C4, C1–22DMB and C1–Bz mixtures is more severe as compared to that in C1–*n*C4, and C1–*n*C6 mixture because it does not matter any more which partner molecule (*i*C4, 22DMB, Bz) blocks the intersection, the reduction is the same; C1 molecules need

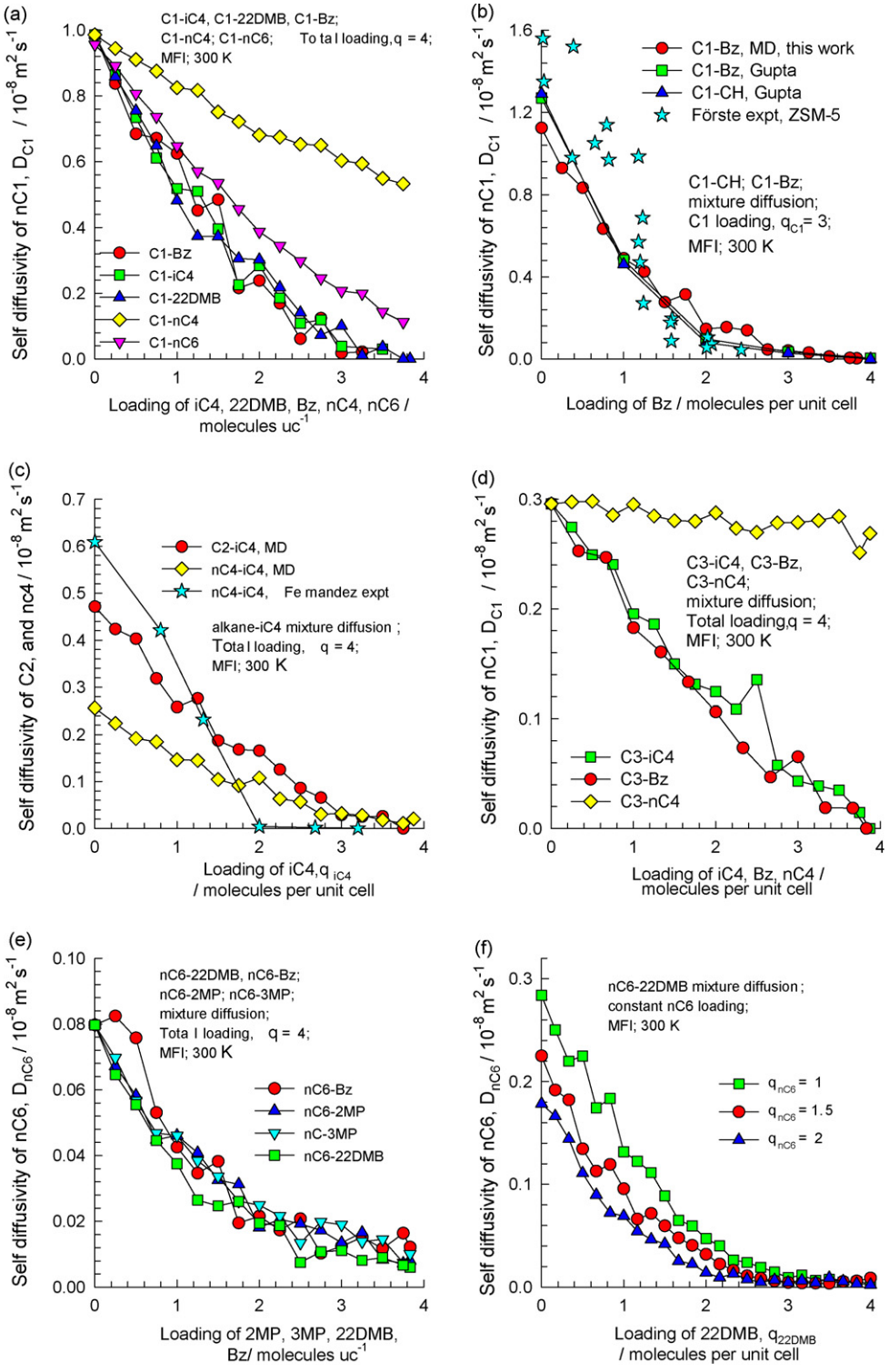

Fig. 5. Self-diffusivities of (a and b) C1, (c) C2, and *n*C4, (d) C3, (e and f) *n*C6 in mixtures with *i*C4, 22DMB, Bz, CH, 3MP or 2MP as a function of the loading of the loading of the partner species.

to by-pass the blocked intersection. For C1–*n*C4 and C1–*n*C6 mixtures, increasing *n*C6 loading has a greater effect on C1 diffusivity than that corresponding to *n*C4. To stress this point further, we compare data for D_{C3} in C3–*i*C4, C3–Bz, and C3–*n*C4 mixtures in Fig. 5d. For C3–*n*C4 mixtures, there is practically no reduction in D_{C3} with increased q_{nC4}. On the other hand, the influence of *i*C4 or Bz is severe, and causes D_{C3} to reduce nearly to zero.

The MD data for D_{nC6} in *n*C6–2MP, *n*C6–3MP, *n*C6–22DMB, and *n*C6–Bz mixtures are presented in Fig. 5e; here the total loading $q = 4$. D_{nC6} shows practically the same dependence on the loading of the partner molecule; intersection blocking by any branched or cyclic hydrocarbon has virtually the same influence on the diffusivity of *n*C6. These results are in qualitative agreement with experimental data for *n*C6–2MP and *n*C6–3MP mixtures [12,13]; a direct comparison with published data is not possible because the loadings inside the zeolite were not measured and the data are presented as a function of gas phase compositions.

Fig. 5f presents MD data for D_{nC6} in *n*C6–22DMB mixtures for which the loading of *n*C6 was held constant at loadings of $q_{nC6} = 1$, 1.5 and 2. The influence of increasing q_{22DMB} is similar in all cases, demonstrating that intersection blocking manifests in a similar fashion irrespective of mixture loading.

The intersection blockage effect can best be appreciated by viewing the animations of the MD simulations [27].

4. Conclusions

Branched or cyclic hydrocarbons such as *i*C4, 2MP, 3MP, 22DMB and Bz adsorb preferentially at the intersections of MFI. This preferential adsorption has two consequences. Firstly, due to the segregated nature of adsorption, the IAST is unable to provide a good quantitative estimate of the component loadings in mixtures. Secondly, the diffusivity of a linear C1–C6 alkane in mixtures with *i*C4, 2MP, 3MP, 22DMB or Bz is severely reduced with increasing loading of its partner molecule; this reduction is due to intersection blocking and is equally deleterious irrespective of which molecule blocks the intersections. Also, the influence of intersection blocking is quantitatively *similar* for all C1–C6 linear alkanes investigated.

There are important consequences of the work reported here in modeling of separation of hydrocarbon mixtures [8,24,28] using an MFI membrane. The strong reduction in the *n*C6 diffusivity due to blockage of the intersections is the one of the causes for the failure of the Maxwell–Stefan (M–S) diffusion equations to provide a good quantitative agreement with experimental data for permeation of *n*C6–3MP mixtures across an MFI membrane, as reported by Zhu et al. [8]. The M–S theory only caters for correlation effects that influence diffusion in hydrocarbon mixtures. Work is in progress to determine ways in which to model intersection blocking using the M–S theory. Another reason for the failure to model the experimental *n*C6–3MP mixture permeation is due to the inability of the IAST to accurately estimate mixture adsorption equilibrium.

Intersection blocking in MFI has consequences in catalysis; it is often observed experimentally that the addition of small amounts of branched hydrocarbons reduces the reactivity of linear hydrocarbons significantly.

Appendix A. Supplementary data

Supplementary data associated with this article can be found, in the online version, at doi:10.1016/j.cej.2007.11.026.

References

[1] H.H. Funke, A.M. Argo, J.L. Falconer, R.D. Noble, Separations of cyclic, branched, and linear hydrocarbon mixtures through silicalite membranes, Ind. Eng. Chem. Res. 36 (1997) 137–143.
[2] C.J. Gump, R.D. Noble, J.L. Falconer, Separation of hexane isomers through nonzeolite pores in ZSM-5 zeolite membranes, Ind. Eng. Chem. Res. 38 (1999) 2775–2781.
[3] J.M. van de Graaf, F. Kapteijn, J.A. Moulijn, Modeling permeation of binary mixtures through zeolite membranes, AIChE J. 45 (1999) 497–511.
[4] M. Arruebo, J.L. Falconer, R.D. Noble, Separation of binary C_5 and C_6 hydrocarbon mixtures through MFI zeolite membranes, J. Membr. Sci. 269 (2006) 171–176.
[5] J. Coronas, R.D. Noble, J.L. Falconer, Separations of C_4 and C_6 isomers in ZSM-5 tubular membranes, Ind. Eng. Chem. Res. 37 (1998) 166–176.
[6] S.K. Gade, V.A. Tuan, C.J. Gump, R.D. Noble, J.L. Falconer, Highly selective separation of *n*-hexane from branched, cyclic and aromatic hydrocarbons using B-ZSM-5 membranes, Chem. Commun. (2001) 601–602.
[7] C.J. Gump, X. Lin, J.L. Falconer, R.D. Noble, Experimental configuration and adsorption effects on the permeation of C_4 isomers through ZSM-5 zeolite membranes, J. Membr. Sci. 173 (2000) 35–52.
[8] W. Zhu, P. Hrabanek, L. Gora, F. Kapteijn, J.C. Jansen, J.A. Moulijn, Modelling of *n*-hexane and 3-methylpentane permeation through a silicalite-1 membrane, Stud. Surf. Sci. Catal. 154 (2004) 1934–1943.
[9] R. Krishna, J.M. van Baten, Diffusion of alkane mixtures in zeolites. Validating the Maxwell–Stefan formulation using MD simulations, J. Phys. Chem. B 109 (2005) 6386–6396.
[10] C. Förste, A. Germanus, J. Kärger, H. Pfeifer, J. Caro, W. Pilz, A. Zikánová, Molecular mobility of methane adsorbed in ZSM-5 containing co-adsorbed benzene, and the location of benzene molecules, J. Chem. Soc., Faraday Trans. 1 83 (1987) 2301–2309.
[11] M. Fernandez, J. Kärger, D. Freude, A. Pampel, J.M. van Baten, R. Krishna, Mixture diffusion in zeolites studied by MAS PFG NMR and molecular simulation, Micropor. Mesopor. Mater. 105 (2007) 124–131.
[12] D. Schuring, A.O. Koriabkina, A.M. de Jong, B. Smit, R.A. van Santen, Adsorption and diffusion of *n*-hexane/2-methylpentane mixtures in zeolite silicalite: experiments and modeling, J. Phys. Chem. B 105 (2001) 7690–7698.
[13] A.O. Koriabkina, A.M. de Jong, D. Schuring, J. van Grondelle, R.A. van Santen, Influence of the acid sites on the intracrystalline diffusion of hexanes and their mixtures within MFI-zeolites, J. Phys. Chem. B 106 (2002) 9559–9566.
[14] T.J.H. Vlugt, W. Zhu, F. Kapteijn, J.A. Moulijn, B. Smit, R. Krishna, Adsorption of linear and branched alkanes in the silicalite-1, J. Am. Chem. Soc. 120 (1998) 5599–5600.
[15] T.J.H. Vlugt, R. Krishna, B. Smit, Molecular simulations of adsorption isotherms for linear and branched alkanes and their mixtures in silicalite, J. Phys. Chem. B 103 (1999) 1102–1118.
[16] R. Krishna, B. Smit, S. Calero, Entropy effects during sorption of alkanes in zeolites, Chem. Soc. Rev. 31 (2002) 185–194.
[17] M. Schenk, S.L. Vidal, T.J.H. Vlugt, B. Smit, R. Krishna, Separation of alkane isomers by exploiting entropy effects during adsorption on silicalite-1: A configurational-bias Monte Carlo simulation study, Langmuir 17 (2001) 1558–1570.
[18] R. Krishna, B. Smit, T.J.H. Vlugt, Sorption-induced diffusion-selective separation of hydrocarbon isomers using silicalite, J. Phys. Chem. A 102 (1998) 7727–7730.

[19] R. Krishna, R. Baur, On the Langmuir–Hinshelwood formulation for zeolite catalysed reactions, Chem. Eng. Sci. 60 (2005) 1155–1166.
[20] A.L. Myers, J.M. Prausnitz, Thermodynamics of mixed gas adsorption, AIChE J. 11 (1965) 121–130.
[21] R. Krishna, S. Calero, B. Smit, Investigation of entropy effects during sorption of mixtures of alkanes in MFI zeolite, Chem. Eng. J. 88 (2002) 81–94.
[22] M. Murthi, R.Q. Snurr, Effects of molecular siting and adsorbent heterogeneity on the ideality of adsorption equilibria, Langmuir 20 (2004) 2489–2497.
[23] R. Krishna, J.M. van Baten, Influence of segregated adsorption on mixture diffusion in DDR zeolite, Chem. Phys. Lett. 446 (2007) 344–349.
[24] R. Krishna, D. Paschek, Separation of hydrocarbon mixtures using zeolite membranes: a modelling approach combining molecular simulations with the Maxwell–Stefan theory, Sep. Purif. Technol. 21 (2000) 111–136.
[25] A. Gupta, R.Q. Snurr, A study of pore blockage in silicalite zeolite using free energy perturbation calculations, J. Phys. Chem. B 109 (2005) 1822–1833.
[26] R. Krishna, J.M. van Baten, Insights into diffusion of gases in zeolites gained from molecular dynamics simulations, Micropor. Mesopor. Mater. 109 (2008) 91–108.
[27] J.M. van Baten, R. Krishna, MD Animations of Diffusion in Zeolites, University of Amsterdam, Amsterdam, October 30, 2007, http://www.science.uva.nl/research/cr/animateMD/.
[28] R. Krishna, R. Baur, Modelling issues in zeolite based separation processes, Sep. Purif. Technol. 33 (2003) 213–254.

Supplementary material to accompany:

Diffusion of hydrocarbon mixtures in MFI zeolite: Influence of intersection blocking

R. Krishna*, J.M. van Baten

Van 't Hoff Institute for Molecular Sciences, University of Amsterdam, Nieuwe Achtergracht 166,

1018 WV Amsterdam, The Netherlands

1. CBMC simulations methodology

CBMC simulations have been carried out to determine the adsorption isotherms for methane (C1), ethane (C2), propane (C3), n-butane (nC4), iso-butane (iC4), n-hexane (nC6), 2-methylpentane (2MP), 3-methylpentane (3MP), and 2,2 dimethyl-butane (22DMB) in MFI (all silica silicalite-1) at 300 K; the crystallographic data are available elsewhere[1, 2]. We use the united atom model. The zeolite framework is considered to be rigid. We consider the CH_x groups as single, chargeless interaction centers with their own effective potentials. The beads in the chain are connected by harmonic bonding potentials. A harmonic cosine bending potential models the bond bending between three neighboring beads, a Ryckaert-Bellemans potential controls the torsion angle. The beads in a chain separated by more than three bonds interact with each other through a Lennard-Jones potential. The Lennard-Jones potentials are shifted and cut at 12 Å. The CBMC simulation details, along with the force fields have been given in detail in earlier publications[3, 4]. The simulation box consists of 2×2×3 unit cells for MFI. Periodic boundary conditions were employed. It was verified that the size of the simulation box was large enough to yield reliable data on adsorption.

Simulations for the adsorption isotherm for benzene (Bz) was carried out with the force field of Ban et al.[5]

Additionally CBMC simulations were carried out to determine the component loadings for various binary mixtures; in these simulations the partial gas phase fugacities were equal, i.e. $f_1 = f_2$.

The CBMC simulations were performed using the BIGMAC code developed by T.J.H. Vlugt[6] as basis.

2. MD simulation methodology

Diffusion is simulated using Newton's equations of motion until the system properties, on average, no longer change in time. The Verlet algorithm is used for time integration. A time step of 1 fs was used in all simulations. For each simulation, *initializing* GCMC moves are used to place the molecules in the

domain, minimizing the energy. Next, follows an *equilibration* stage. These are essentially the same as the production cycles, only the statistics are not yet taken into account. This removes any initial large disturbances in the system do not affect statistics. After a fixed number of initialization and equilibrium steps, the MD simulation *production* cycles start. For every cycle, the statistics for determining the mean square displacements (MSDs) are updated. The MSDs are determined for time intervals ranging from 2 fs to 1 ns. In order to do this, an order-*N* algorithm, as detailed in Chapter 4 of Frenkel and Smit[7] is implemented. The Nosé-Hoover thermostat is applied to all the diffusing particles.

The DLPOLY code[8] was used along with the force field implementation as described in the previous section. DL_POLY is a molecular dynamics simulation package written by W. Smith, T.R. Forester and I.T. Todorov and has been obtained from CCLRCs Daresbury Laboratory via the website.[8]

The MD simulations were carried out for a variety of molecular loadings. All simulations were carried out on clusters of PCs equipped with Intel Xeon processors running at 3.4 GHz on the Linux operating system. Each MD simulation, for a specified loading, was run for 120 h, determined to be long enough to obtain reliable statistics for determination of the diffusivities. Several independent MD simulations were run and the results averaged.

The self-diffusivities, $D_{\mathrm{i,self}}$, were computed by analyzing the mean square displacement of each species *i* for each of the coordinate directions:

$$D_{i,self} = \frac{1}{2n_i} \lim_{\Delta t \to \infty} \frac{1}{\Delta t} \left\langle \left(\sum_{l=1}^{n_i} \left(\mathbf{r}_{l,i}(t + \Delta t) - \mathbf{r}_{l,i}(t) \right)^2 \right) \right\rangle \qquad (1)$$

In this expression n_{i} represents the number of molecules of species *i* respectively, and $\mathbf{r}_{\mathrm{l,i}}(t)$ is the position of molecule *l* of species *i* at any time *t*. The expression (1) also defines the self-diffusivity in a *n*-component mixture.

In the Maxwell-Stefan (M-S) formulation the flux of any species in a binary mixture is related to its chemical potential gradient by [9]

$$-\rho\frac{\theta_i}{RT}\frac{d\mu_i}{dx}=\sum_{\substack{j=1\\ j\neq i}}^{n}\frac{q_j N_i - q_i N_j}{q_{i,sat}q_{j,sat}Đ_{ij}}+\frac{N_i}{q_{i,sat}Đ_i};\quad i=1,...n \tag{2}$$

where N_i is the molar flux, ρ is the zeolite framework density, q_i is the molar loading, $q_{i,sat}$ is the saturation capacity, $d\mu_i/dx$ is the chemical potential gradient, R is the gas constant, T is the absolute temperature, $Đ_i$ is the M-S diffusivity, and $Đ_{ij}$ are the binary exchange coefficients. Conformity with the Onsager Reciprocal Relations demands that

$$q_{j,sat}Đ_{ij}=q_{i,sat}Đ_{ji} \tag{3}$$

The gradient of the chemical potentials in eq (2) can be related to the gradients in the loadings by defining a 2×2 dimensional matrix of thermodynamic factors [Γ]

$$\frac{q_i}{RT}\frac{d\mu_i}{dx}=\sum_{j=1}^{2}\Gamma_{ij}\frac{dq_j}{dx};\quad \Gamma_{ij}\equiv\frac{q_i}{f_i}\frac{\partial f_i}{\partial q_j};\quad i,j=1,2 \tag{4}$$

The elements Γ_{ij} in eq (4) can be estimated, for example, using the Ideal Adsorbed Solution Theory of Myers and Prausnitz [10] and the fits of the pure component isotherm data. The fluxes N_i can be explicitly expressed as functions of the gradients in the loading

$$(N)=-\rho[\Delta][\Gamma]\frac{d(q)}{dx} \tag{5}$$

where [Δ] is a square matrix of M-S diffusivities. Compliance with the Onsager Reciprocal Relations demands that

$$q_2\Delta_{12}=q_1\Delta_{21} \tag{6}$$

The diagonal elements Δ_{ii} in each of the coordinate directions for the linear alkanes were obtained from

$$\Delta_{ii}=\frac{1}{2}\lim_{\Delta t\to\infty}\frac{1}{n_i}\frac{1}{\Delta t}\left\langle\left(\sum_{l=1}^{n_i}\left(\mathbf{r}_{l,i}(t+\Delta t)-\mathbf{r}_{l,i}(t)\right)\right)^2\right\rangle \tag{7}$$

In this expression n_i represents the number of molecules of species i, and $\mathbf{r}_{l,i}(t)$ is the position of molecule l of species i at any time t.

The values of Δ_{ii} for the branched alkanes and Bz are about 2-3 orders of magnitude lower than that of the linear alkanes; these are too low to be accurately determined from MD simulations and are not reported in the paper.

3. Simulation results

Snapshots showing the location of the molecules within the intersecting channel structures of MFI are shown in Figures 1 - 12. Alongside the snapshots are comparisons of CBMC simulations of pure component isotherms with published experimental data in MFI.

The CBMC simulated pure component isotherms were fitted with a 3-site Langmuir model

$$q = \frac{q_{sat,A} b_A f}{1 + b_A f} + \frac{q_{sat,B} b_B f}{1 + b_B f} + \frac{q_{sat,C} b_C f}{1 + b_C f} \qquad (8)$$

In eq. (8) q is the molar loading expressed in mol kg^{-1}, $q_{sat,A}$ is the saturation loading of site A, and f is the fugacity of the bulk gas phase. The values of the fitted parameters b and q_{sat} are specified in Table 1. Note that 1 molecule per unit cell equals a loading of 0.6935 mol kg^{-1}.

For C1-iC4 mixture the pure component isotherms determined from CBMC simulations, along with the 3-site Langmuir fits are shown in Figure 13. Also shown are the CBMC simulated component loadings of the adsorbed phase in equilibrium with an equimolar gas mixture with varying fugacities. The CBMC simulations are compared with the IAST [10] predictions (shown by continuous solid lines). Figure 14 shows snasphots (top view and side view) of the location of C1 and iC4 in MFI channels. The side view is 3 unit cells deep and the top view is 2 unit cells deep. On the right side in Figure 14 are presented the self-diffusivities $D_{i,self}$ and diagonal Δ_{ii} of C1 in the three coordinate directions of MFI.

The data for all other mixtures are given in Figures 15 –36.

4. References

[1] C. Baerlocher, L.B. McCusker, Database of Zeolite Structures, International Zeolite Association, http://www.iza-structure.org/databases/, 26 June 2001.

[2] J.M. van Baten, R. Krishna, MD Simulations of Diffusion in Zeolites, University of Amsterdam, http://www.science.uva.nl/research/cr/md/,

[3] D. Dubbeldam, S. Calero, T.J.H. Vlugt, R. Krishna, T.L.M. Maesen, E. Beerdsen, B. Smit, Force Field Parametrization through Fitting on Inflection Points in Isotherms, Phys. Rev. Lett. 93 (2004) 088302.

[4] D. Dubbeldam, S. Calero, T.J.H. Vlugt, R. Krishna, T.L.M. Maesen, B. Smit, United Atom Forcefield for Alkanes in Nanoporous Materials, J. Phys. Chem. B 108 (2004) 12301-12313.

[5] S. Ban, A. van Laak, P.E. de Jongh, J.P.J.M. van der Eerden, T.J.H. Vlugt, Adsorption Selectivity of Benzene and Propene Mixtures for Various Zeolites, J. Phys. Chem. C 111 (2007) 17241-17248.

[6] T.J.H. Vlugt, BIGMAC, University of Amsterdam, http://molsim.chem.uva.nl/bigmac/, 1 November 2000.

[7] D. Frenkel, B. Smit, Understanding molecular simulations: from algorithms to applications, Academic Press, 2nd Edition, San Diego, 2002.

[8] W. Smith, T.R. Forester, I.T. Todorov, The DL_POLY Molecular Simulation Package, Warrington, England, http://www.cse.clrc.ac.uk/msi/software/DL_POLY/index.shtml, March 2006.

[9] R. Krishna, J.M. van Baten, Diffusion of alkane mixtures in zeolites. Validating the Maxwell-Stefan formulation using MD simulations, J. Phys. Chem. B 109 (2005) 6386-6396.

[10] A.L. Myers, J.M. Prausnitz, Thermodynamics of mixed gas adsorption, A.I.Ch.E.J. 11 (1965) 121-130.

[11] M.S. Sun, D.B. Shah, H.H. Xu, O. Talu, Adsorption equilibria of C_1 to C_4 alkanes, CO_2, and SF_6 on silicalite, J. Phys. Chem. B 102 (1998) 1466-1473.

[12] W. Zhu, F. Kapteijn, J.A. Moulijn, Adsorption of light alkanes on silicalite-1: Reconciliation of experimental data and molecular simulations, Phys. Chem. Chem. Phys. 2 (2000) 1989-1995.

[13] T.C. Golden, S. Sircar, Gas Adsorption on Silicalite, J. Colloid Interface Sci. 162 (1994) 182-188.

[14] M. Kishima, H. Mizuhata, T. Okubo, Effects of Confinement on the Adsorption Behavior of Methane in High-Silica Zeolites, J. Phys. Chem. B 110 (2006) 13889-13896.

[15] B. Millot, A. Methivier, H. Jobic, Adsorption of n-alkanes on silicalite crystals. A temperature-programmed desorption study, J. Phys. Chem. B 102 (1998) 3210-3215.

[16] L. Song, L.V.C. Rees, Adsorption and transport of n-hexane in siliaclite-1 by the frequency response technique, J. Chem. Soc.-Faraday Trans. 93 (1997) 649-657.

[17] C.L. Cavalcante, D.M. Ruthven, Adsorption of Branched and Cyclic Paraffins in Silicalite.1. Equilibrium, Ind. Eng. Chem. Res. 34 (1995) 177-184.

[18] W. Zhu, F. Kapteijn, B. van der Linden, J.A. Moulijn, Equilibrium adsorption of linear and branched C_6 alkanes on silicalite-1 studied by the tapered element oscillating microbalance, Phys. Chem. Chem. Phys. 3 (2001) 1755-1761.

[19] E. Jolimaitre, M. Tayakout-Fayolle, C. Jallut, K. Ragil, Determination of mass transfer and thermodynamic properties of branched paraffins in silicalite by inverse chromatography technique, Ind. Eng. Chem. Res. 40 (2001) 914-926.

Table 1. Three-site Langmuir parameters for pure component isotherms in MFI at 300 K. The saturation capacity q_{sat} has the units of mol kg^{-1}. The Langmuir parameters b_i, have the units of Pa^{-1}.

Molecule	Three-Site Langmuir parameters					
	b_A	$q_{sat,A}$	b_B	$q_{sat,B}$	b_C	$q_{sat,C}$
C1	3.25×10^{-6}	2.8	2.2×10^{-8}	0.7	1.12×10^{-10}	0.5
C2	9.3×10^{-5}	2.2	5×10^{-7}	0.63	-	-
C3	9.97×10^{-4}	1.9	6.61×10^{-6}	0.16	-	-
nC4	1.9×10^{-2}	0.8	8×10^{-3}	0.77	9.3×10^{-6}	0.17
iC4	2.4×10^{-2}	0.693	2.86×10^{-5}	1.04	-	-
nC6	2.33	0.693	1.61	0.347	8.87×10^{-2}	0.347
2MP	4.64	0.693	2.92×10^{-5}	0.693	-	-
3MP	1.53	0.693	2.69×10^{-3}	0.381	2.19×10^{-5}	0.312
22DMB	0.545	0.693	-	-	-	-
Bz	0.155	0.693	1.66×10^{-6}	0.693	1.32×10^{-4}	0.61

5. Captions for Figures

Figure 1. Snapshots of C1, along with comparison of CBMC simulations with experimental data [11-14].

Figure 2. Snapshots of C2, along with comparison of CBMC simulations with experimental data [11].

Figure 3. Snapshots of C3, along with comparison of CBMC simulations with experimental data [11].

Figure 4. Snapshots of nC4, along with comparison of CBMC simulations with experimental data [11].

Figure 5. Snapshots of iC4 at loadings of 2 and 4 molecules per unit cell in MFI.

Figure 6. Snapshots of iC4 at loadings of 6 molecules per unit cell, along with comparison of CBMC simulations with experimental data [11, 12].

Figure 7. Snapshots of nC6, along with comparison of CBMC simulations with experimental data [15, 16].

Figure 8. Snapshots of 22DMB, along with comparison of CBMC simulations with experimental data[17].

Figure 9. Snapshots of 2MP , along with comparison of CBMC simulations with experimental data[18].

Figure 10. Snapshots of 3MP, along with comparison of CBMC simulations with experimental data[18, 19].

Figure 11. Snapshots of Benzene at loadings of 1, and 2 molecules per unit cell in MFI.

Figure 12. Snapshots of Benzene at loadings of 3, and 4 molecules per unit cell in MFI.

Figure 13. Pure component and binary adsorption data for C1-iC4 binary mixture. For binary mixture adsorption, the CBMC simulation results are compared with IAST predictions using the pure component isotherm fits.

Figure 14. Snasphots (top view and side view) showing location of C1 and iC4 in MFI channels. The side view is 2 unit cells deep and the top view is 2 unit cells deep. On the right side are presented the self-diffusivities $D_{i,self}$ and diagonal Δ_{ii} of C1 in the three coordinate directions of MFI.

Figure 15. Pure component and binary adsorption data for C2-iC4 binary mixture.

Figure 16. Snasphots (top view and side view) showing location of C2 and iC4 in MFI channels. The side view is 2 unit cells deep and the top view is 2 unit cells deep. On the right side are presented the self-diffusivities $D_{i,self}$ and diagonal Δ_{ii} of C2 in the three coordinate directions of MFI.

Figure 17. Pure component and binary adsorption data for C3-iC4 binary mixture.

Figure 18. Snasphots (top view and side view) showing location of C3 and iC4 in MFI channels. The side view is 2 unit cells deep and the top view is 2 unit cells deep. On the right side are presented the self-diffusivities $D_{i,self}$ and diagonal Δ_{ii} of C3 in the three coordinate directions of MFI.

Figure 19. Pure component and binary adsorption data for nC4-iC4 binary mixture.

Figure 20. Snasphots (top view and side view) showing location of nC4 and iC4 in MFI channels. The side view is 2 unit cells deep and the top view is 2 unit cells deep. On the right side are presented the self-diffusivities $D_{i,self}$ and diagonal Δ_{ii} of nC4 in the three coordinate directions of MFI.

Figure 21. Pure component and binary adsorption data for C1-Bz binary mixture.

Figure 22. Snasphots (top view and side view) showing location of C1 and Bz in MFI channels. The side view is 3 unit cells deep and the top view is 2 unit cells deep. On the right side are presented the self-diffusivities $D_{i,self}$ and diagonal Δ_{ii} of C1 in the three coordinate directions of MFI.

Figure 23. Pure component and binary adsorption data for C1-22DMB binary mixture.

Figure 24. Snasphots (top view and side view) showing location of C1 and 22DMB in MFI channels. The side view is 3 unit cells deep and the top view is 2 unit cells deep. On the right side are presented the self-diffusivities $D_{i,self}$ and diagonal Δ_{ii} of C1 in the three coordinate directions of MFI.

Figure 25. Pure component and binary adsorption data for C3-Bz binary mixture.

Figure 26. Snasphots (top view and side view) showing location of C3 and Bz in MFI channels. The side view is 3 unit cells deep and the top view is 2 unit cells deep. On the right side are presented the self-diffusivities $D_{i,self}$ and diagonal Δ_{ii} of C3 in the three coordinate directions of MFI.

Figure 27. Pure component and binary adsorption data for nC6-22DMB binary mixture.

Figure 28. Snasphots (top view and side view) showing location of nC6 and 22DMB in MFI channels. The side view is 3 unit cells deep and the top view is 2 unit cells deep. On the right side are presented the self-diffusivities $D_{i,self}$ and diagonal Δ_{ii} of nC6 in the three coordinate directions of MFI

Figure 29. Diffusivities in binary mixtures of nC6 and 22DMB in MFI channels in which the nC6 loading is kept constant; q_{nC6}= 1, and 1.5 and the loading of 22DMB is varied.

Figure 30. Diffusivities in binary mixtures of nC6 and 22DMB in MFI channels in which the nC6 loading is kept constant; q_{nC6}= 2, and the loading of 22DMB is varied.

Figure 31. Pure component and binary adsorption data for nC6-Bz binary mixture.

Figure 32. Snasphots (top view and side view) showing location of nC6 and Bz in MFI channels. The side view is 3 unit cells deep and the top view is 2 unit cells deep. On the right side are presented the self-diffusivities $D_{i,self}$ and diagonal Δ_{ii} of nC6 in the three coordinate directions of MFI.

Figure 33. Pure component and binary adsorption data for nC6-2MP binary mixture.

Figure 34. Snasphots (top view and side view) showing location of nC6 and 2MP in MFI channels. The side view is 3 unit cells deep and the top view is 2 unit cells deep. On the right side are presented the self-diffusivities $D_{i,self}$ and diagonal Δ_{ii} of nC6 in the three coordinate directions of MF.I

Figure 35. Pure component and binary adsorption data for nC6-3MP binary mixture.

Figure 36. Snasphots (top view and side view) showing location of nC6 and 3MP in MFI channels. The side view is 3 unit cells deep and the top view is 2 unit cells deep. On the right side are presented the self-diffusivities $D_{i,self}$ and diagonal Δ_{ii} of nC6 in the three coordinate directions of MFI.

Figure 1

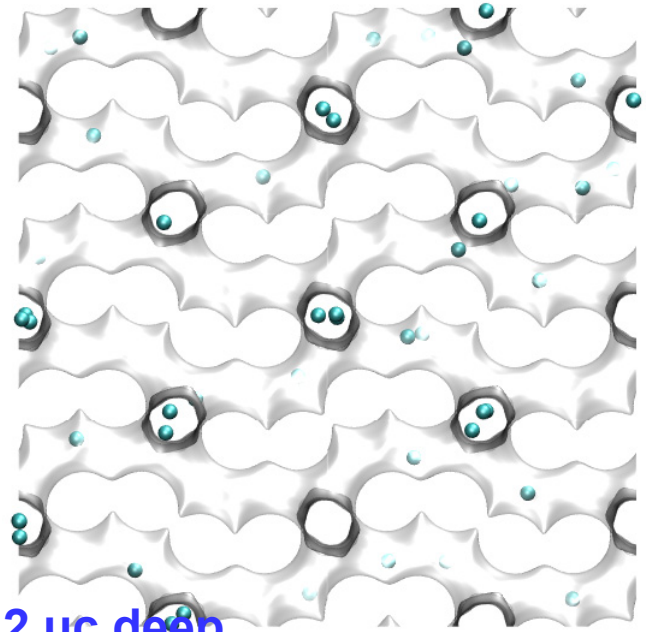

2 uc deep

C1: 4 molecules/uc

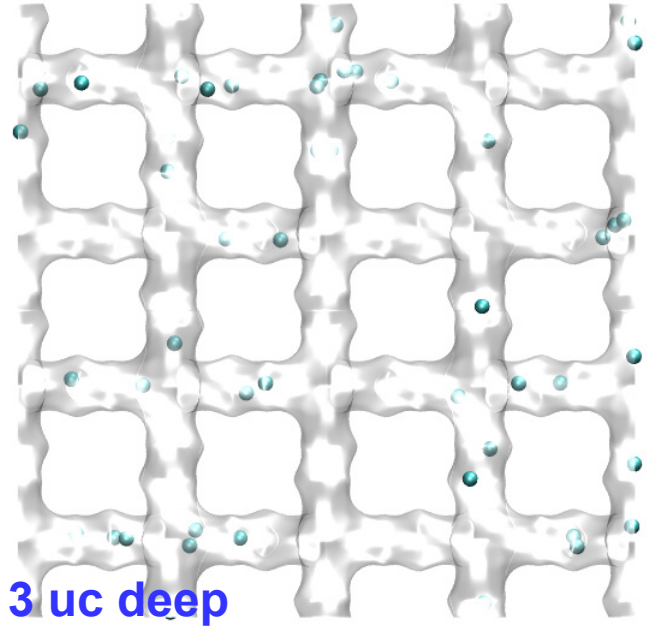

3 uc deep

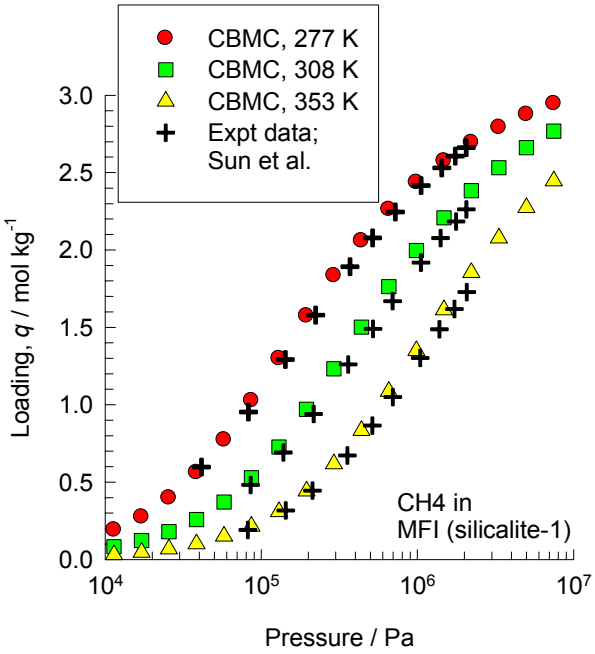

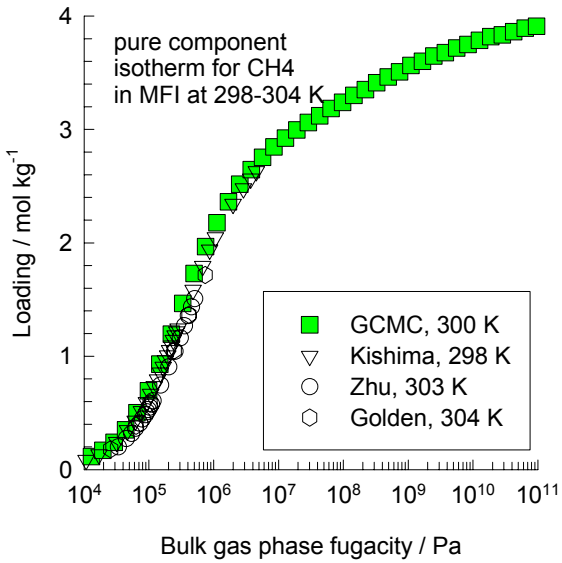

Figure 2

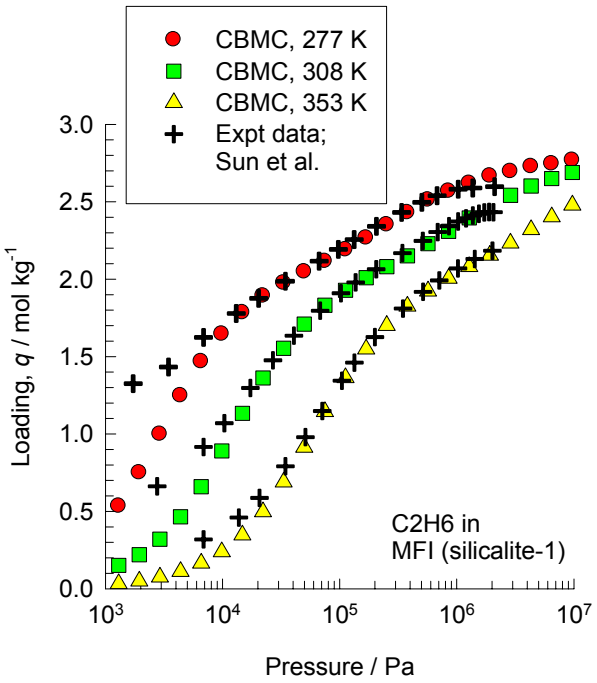

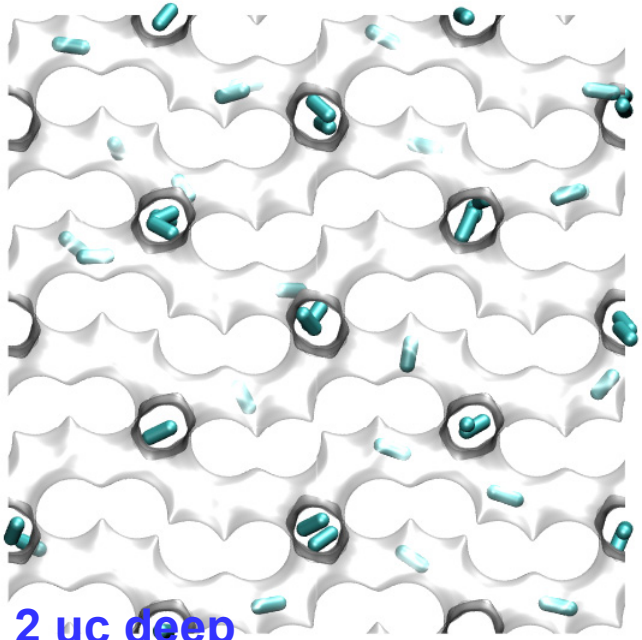

C2: 4 molecules/uc

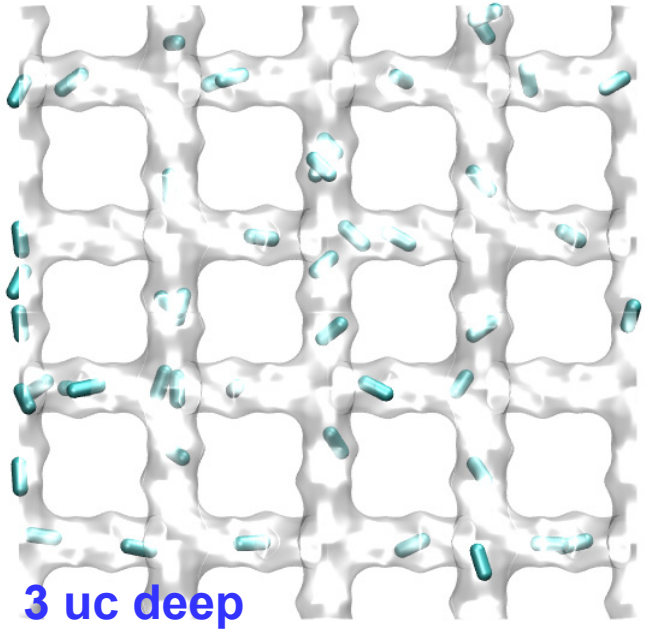

Figure 3

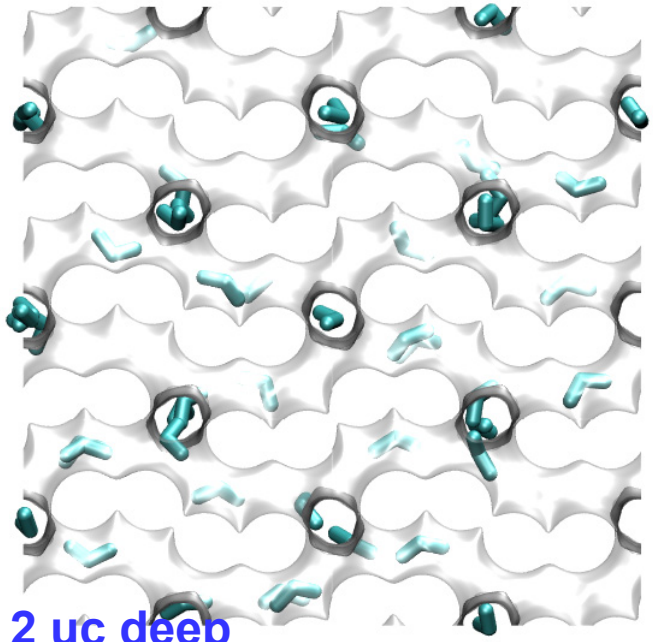

2 uc deep

C3: 4 molecules/uc

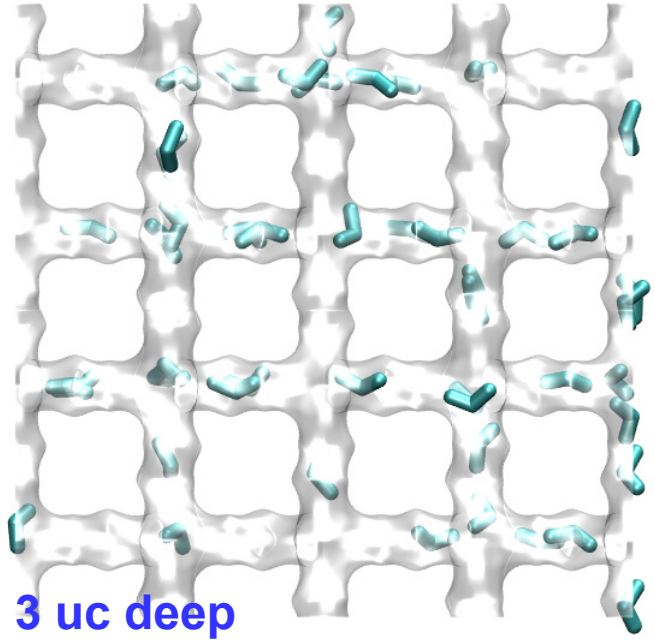

3 uc deep

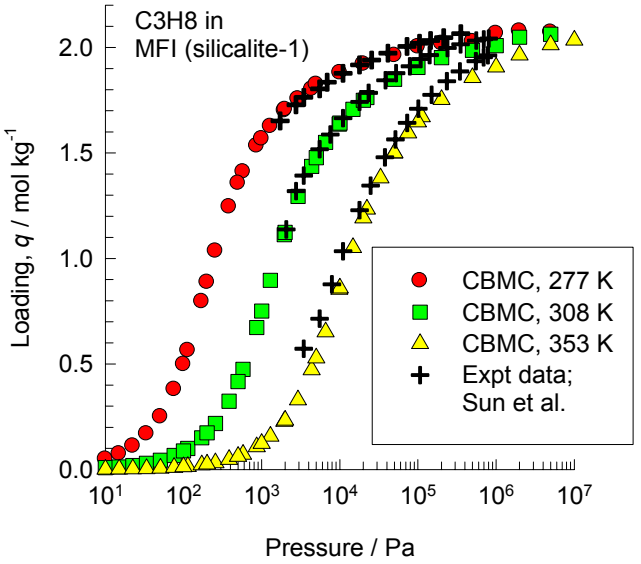

Figure 4

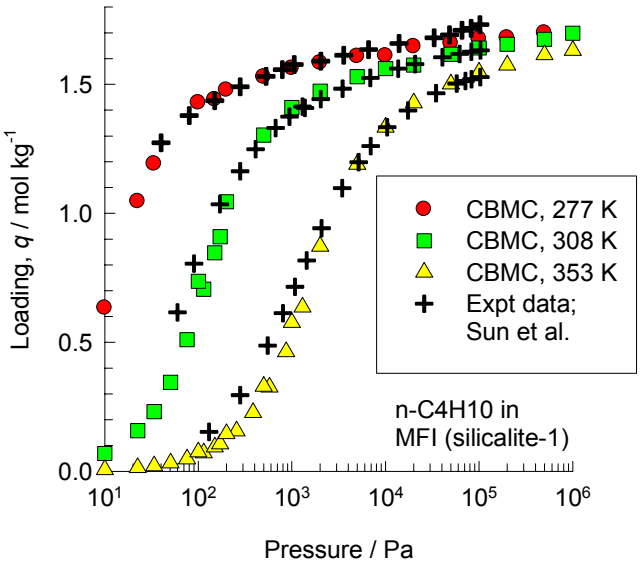

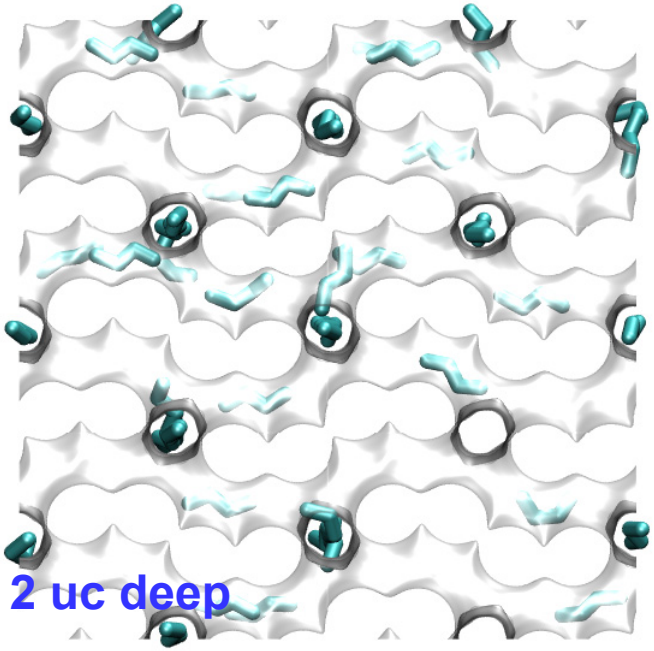

nC4: 4 molecules/uc

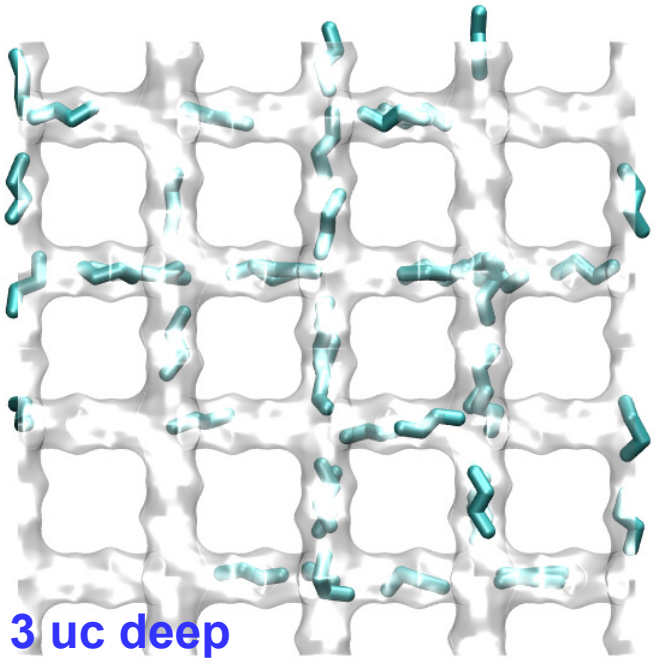

Figure 5

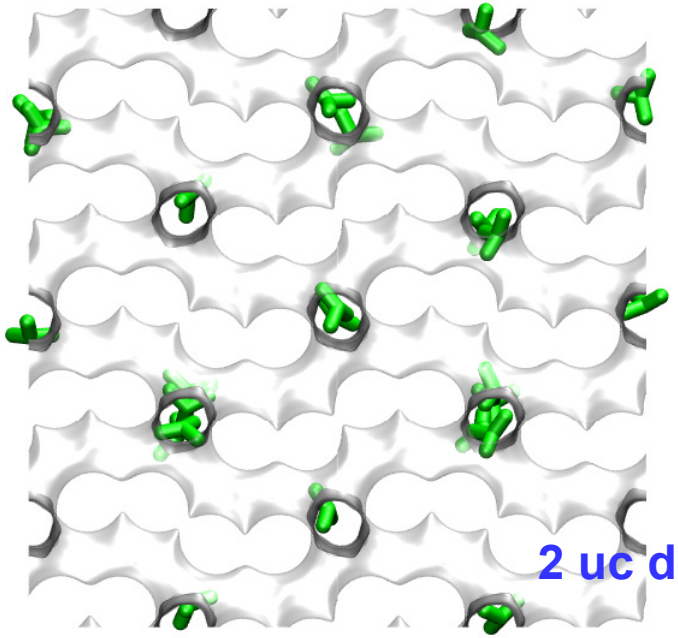

2 uc deep

2 uc deep

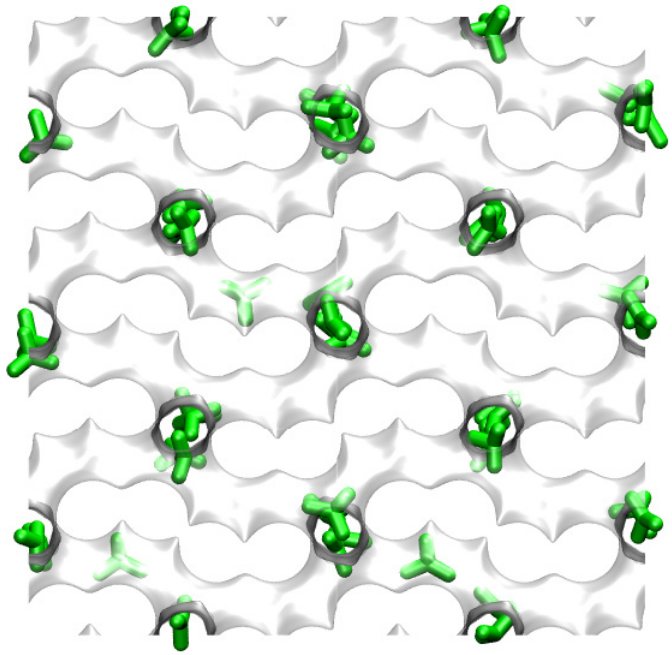

iC4: 2 molecules/uc

iC4: 4 molecules/uc

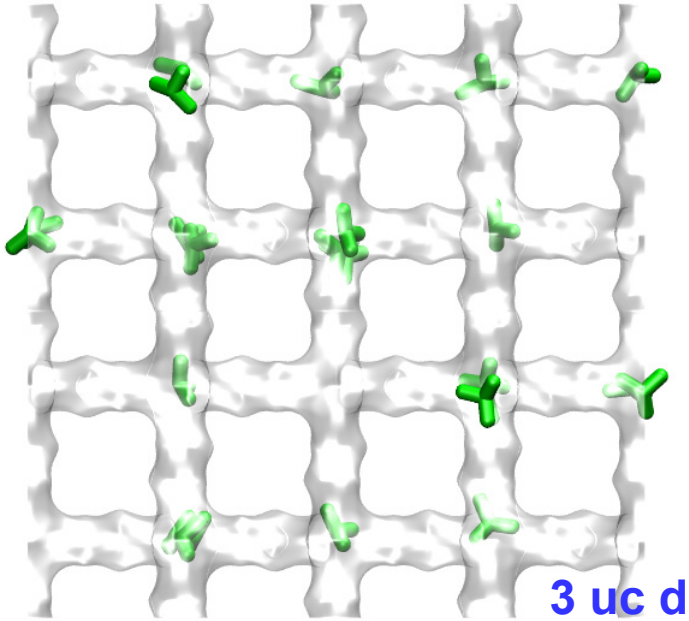

3 uc deep

3 uc deep

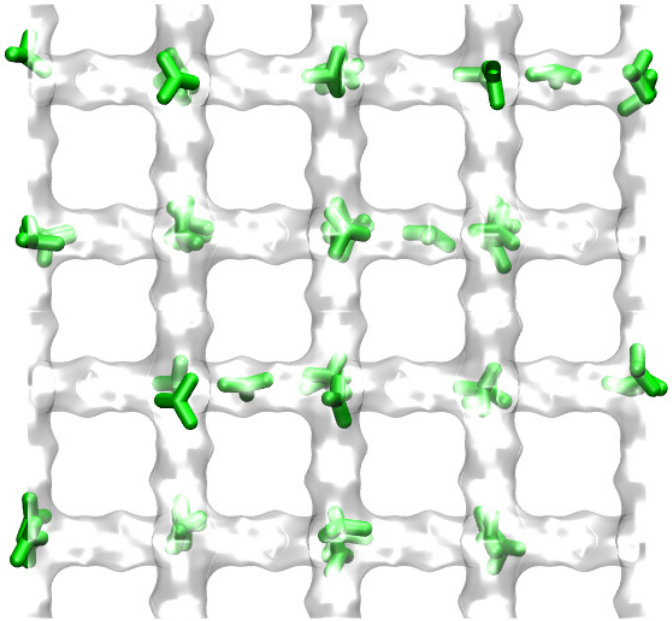

Figure 6

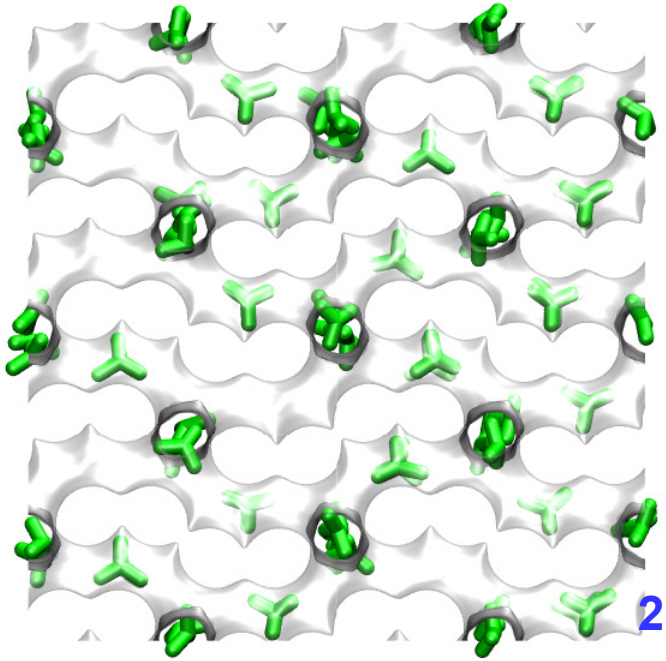

2 uc deep

iC4: 6 molecules/uc

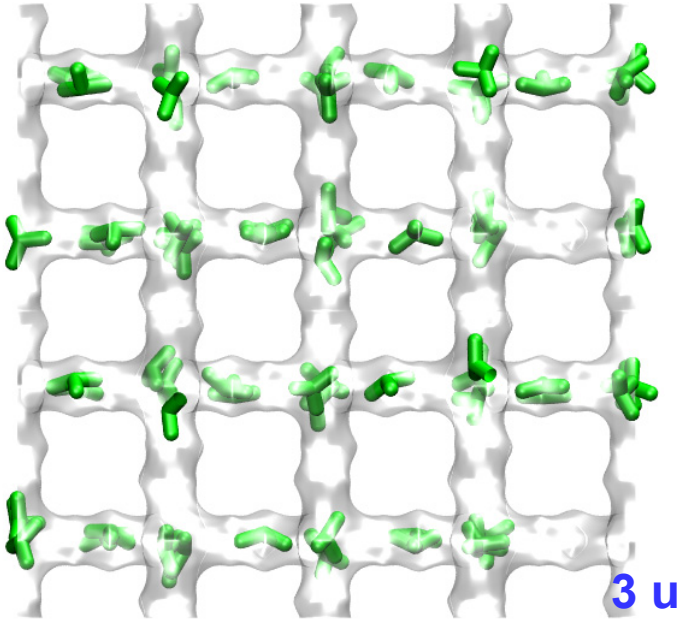

3 uc deep

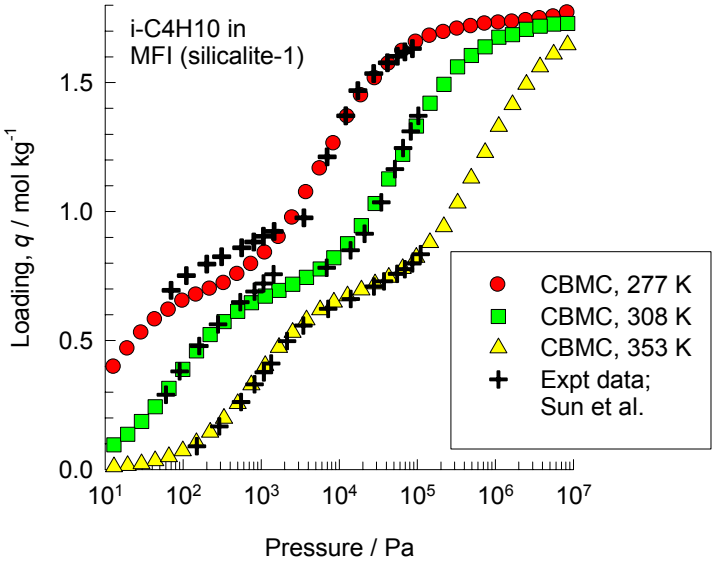

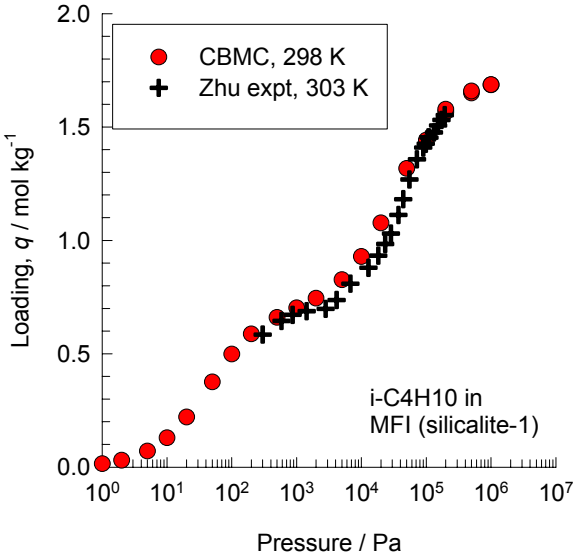

Figure 7

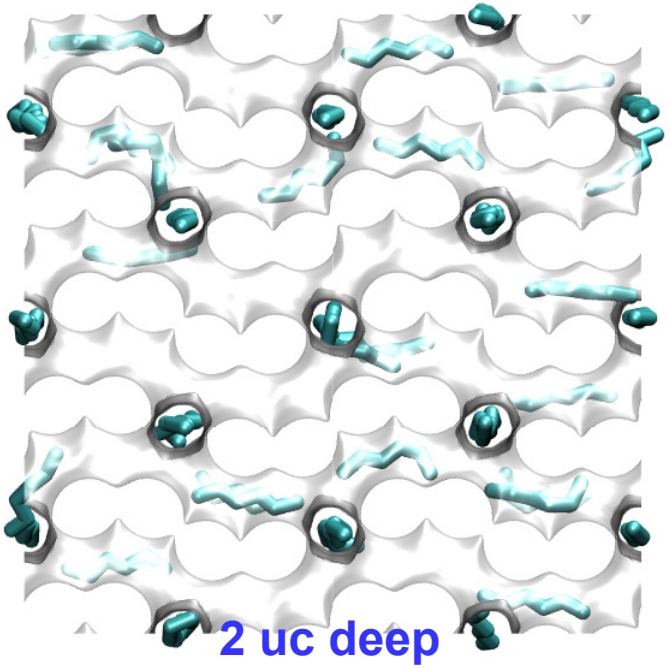
2 uc deep
nC6: 4 molecules/uc
3 uc deep

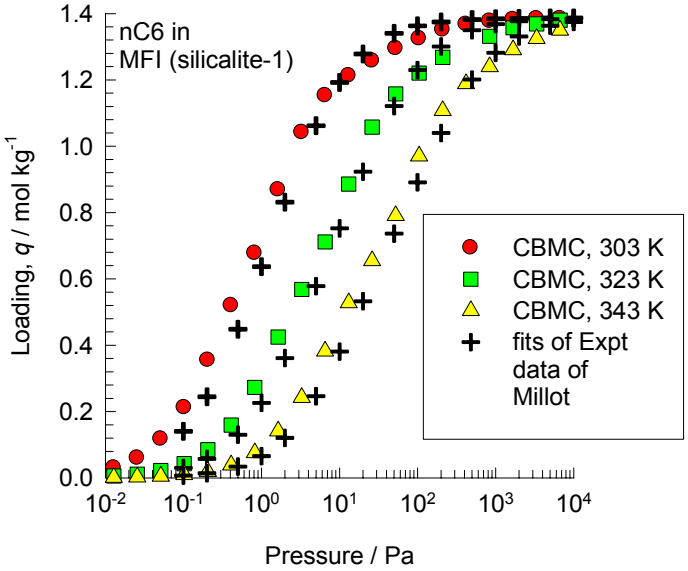
nC6 in
MFI (silicalite-1)
Loading, q / mol kg-1
Pressure / Pa
CBMC, 303 K
CBMC, 323 K
CBMC, 343 K
fits of Expt data of Millot

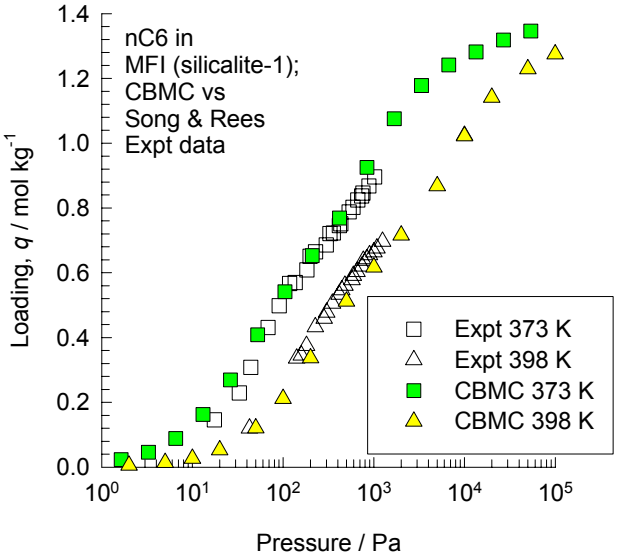
nC6 in
MFI (silicalite-1);
CBMC vs
Song & Rees
Expt data
Loading, q / mol kg-1
Pressure / Pa
Expt 373 K
Expt 398 K
CBMC 373 K
CBMC 398 K

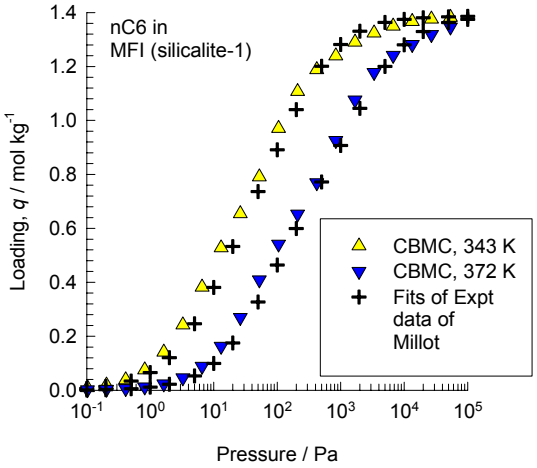
nC6 in
MFI (silicalite-1)
Loading, q / mol kg-1
Pressure / Pa
CBMC, 343 K
CBMC, 372 K
Fits of Expt data of Millot

Figure 8

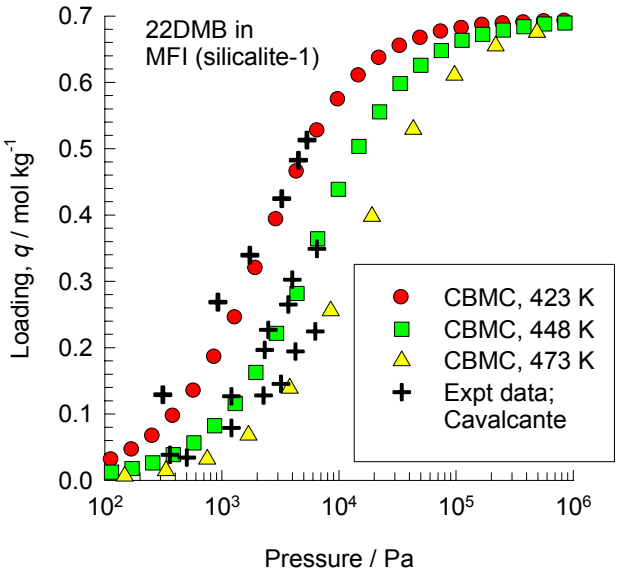
22DMB in
MFI (silicalite-1)
Loading, q / mol kg-1
Pressure / Pa
CBMC, 423 K
CBMC, 448 K
CBMC, 473 K
Expt data;
Cavalcante

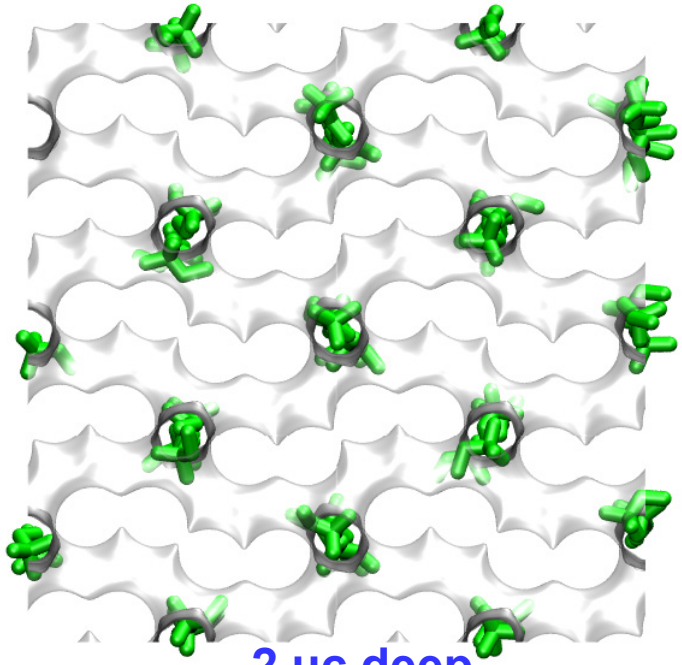
2 uc deep
22DMB: 4 molecules/uc

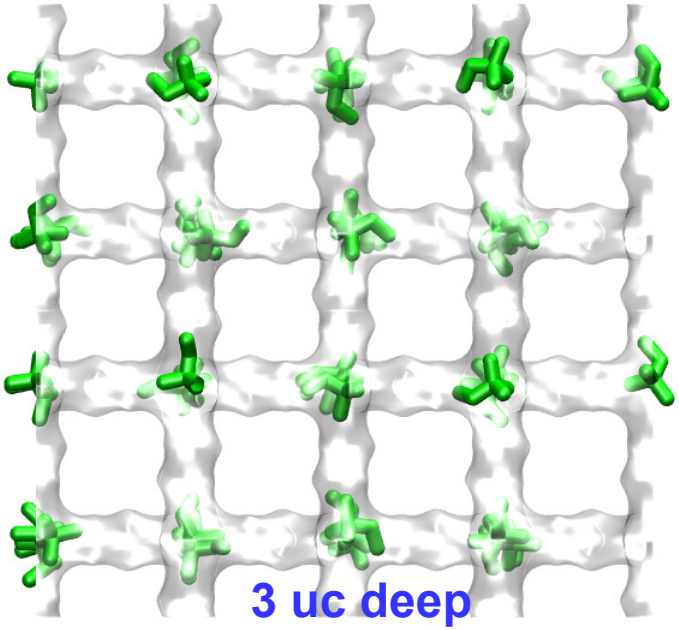
3 uc deep

Figure 9

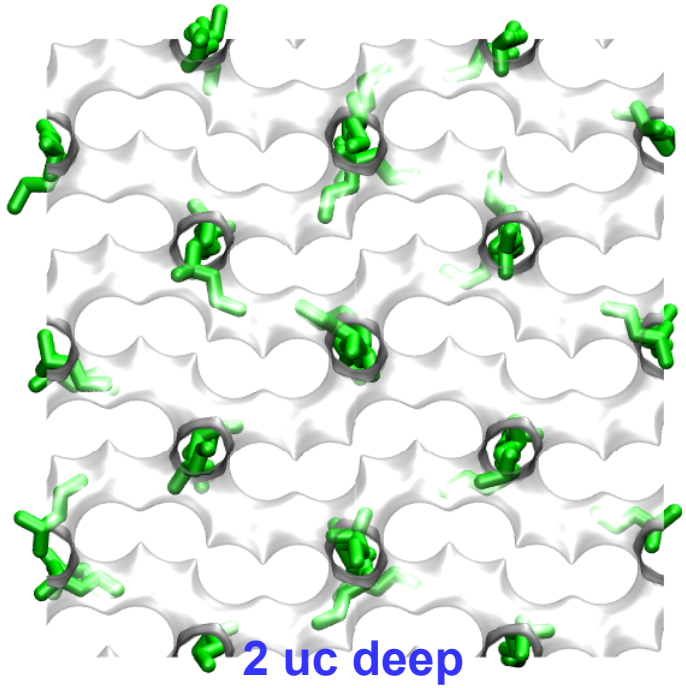
2 uc deep
2MP: 4 molecules/uc

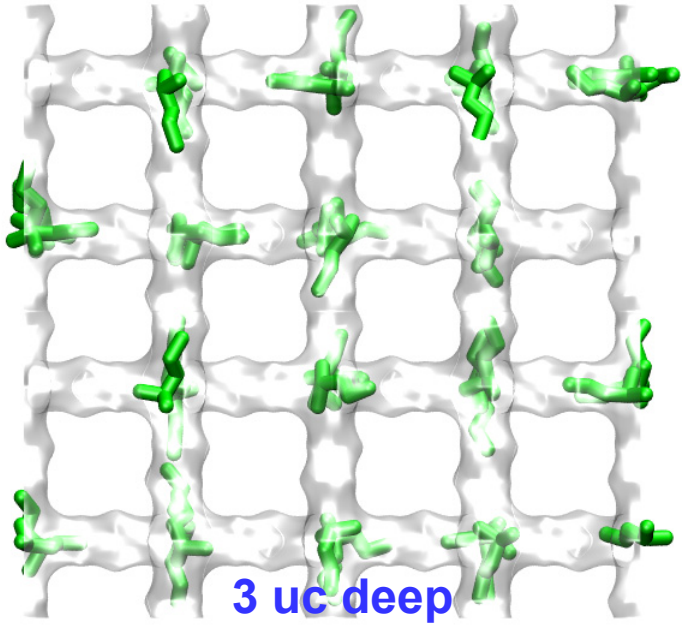
3 uc deep

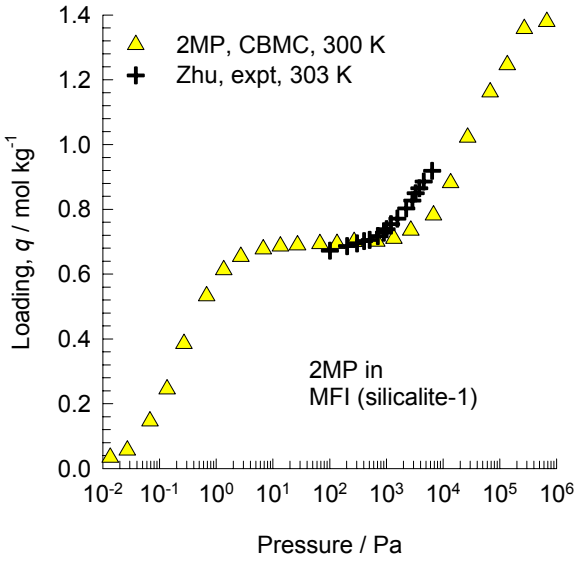
2MP, CBMC, 300 K
Zhu, expt, 303 K
2MP in
MFI (silicalite-1)
Loading, q / mol kg-1
Pressure / Pa
0.0
0.2
0.4
0.6
0.8
1.0
1.2
1.4
10-2
10-1
100
101
102
103
104
105
106

Figure 10

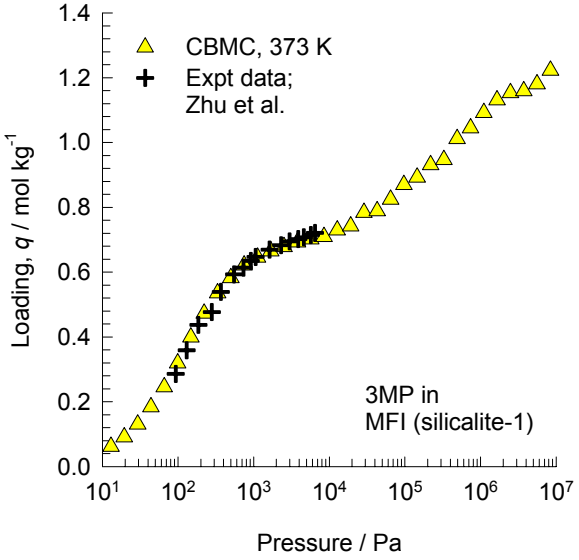

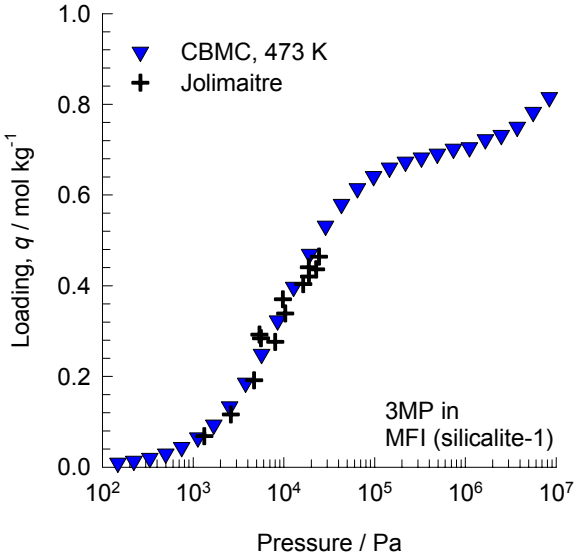

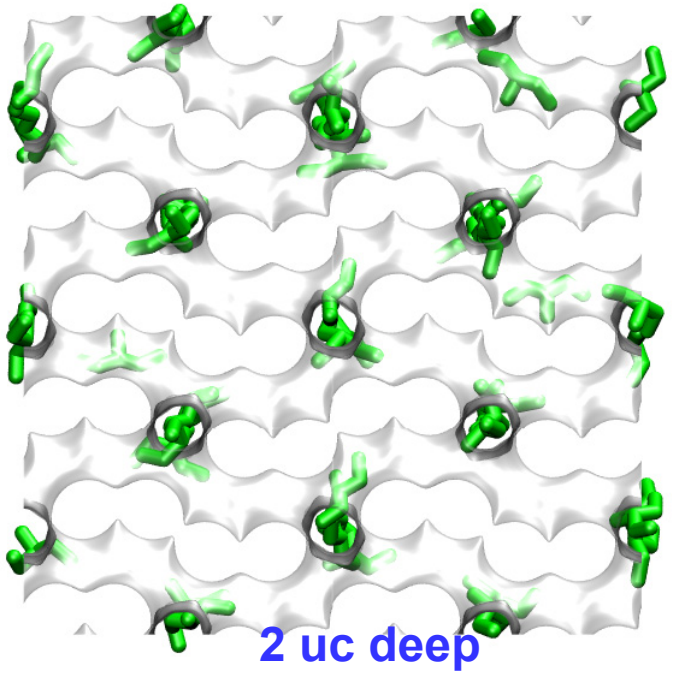

3MP: 4 molecules/uc

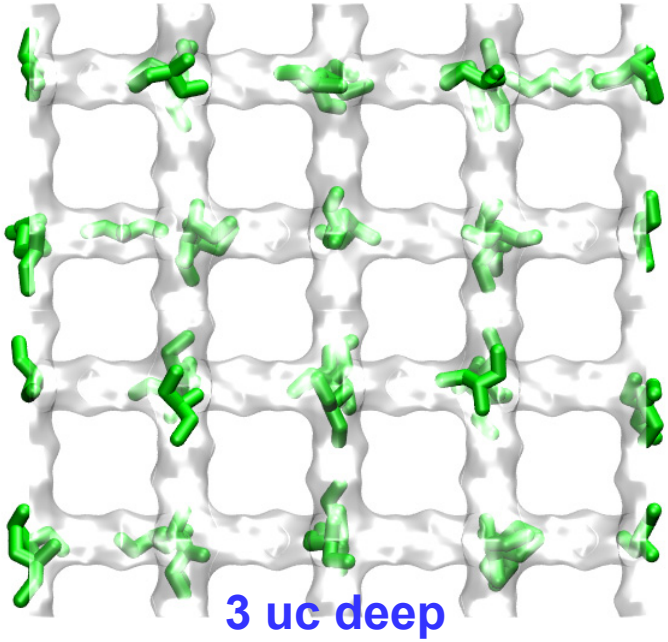

Figure 11

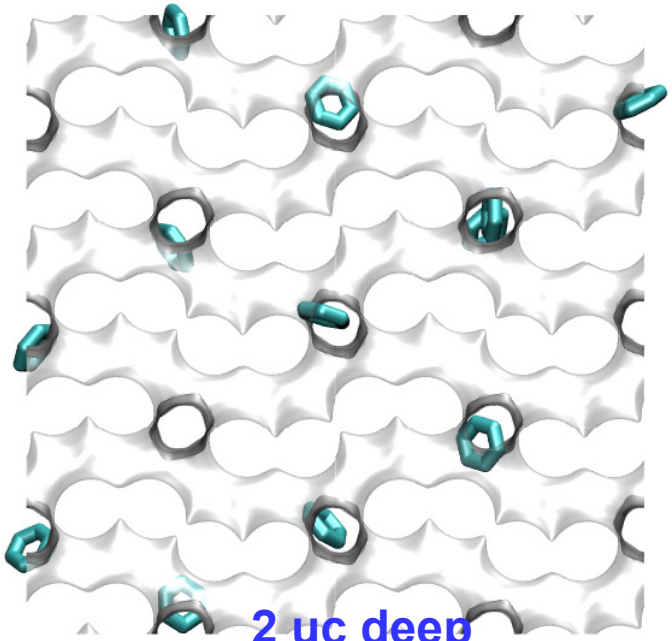

Benzene: 1 molecules/uc

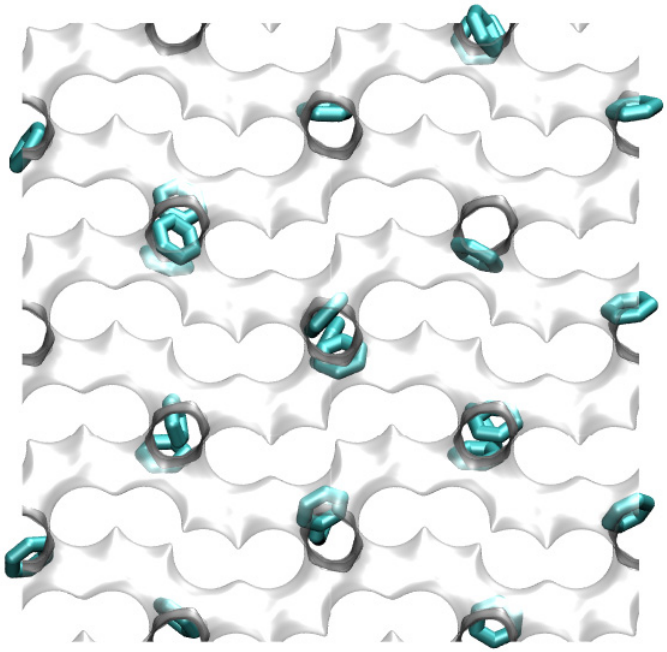

Benzene: 2 molecules/uc

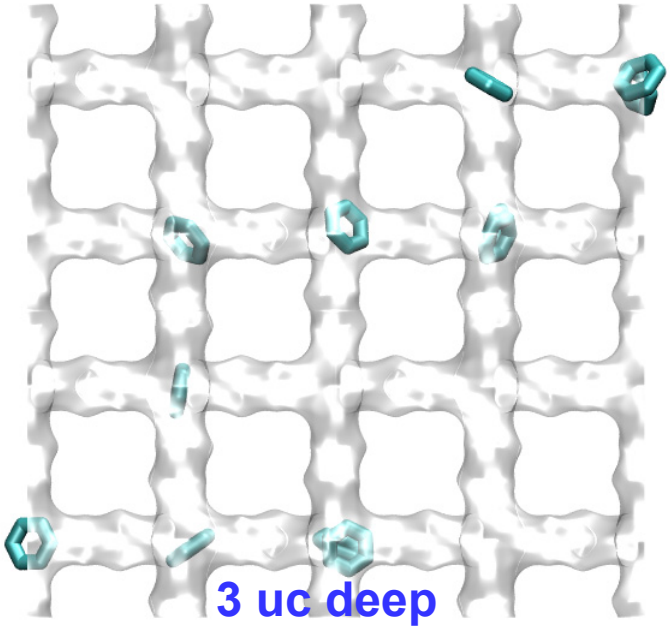

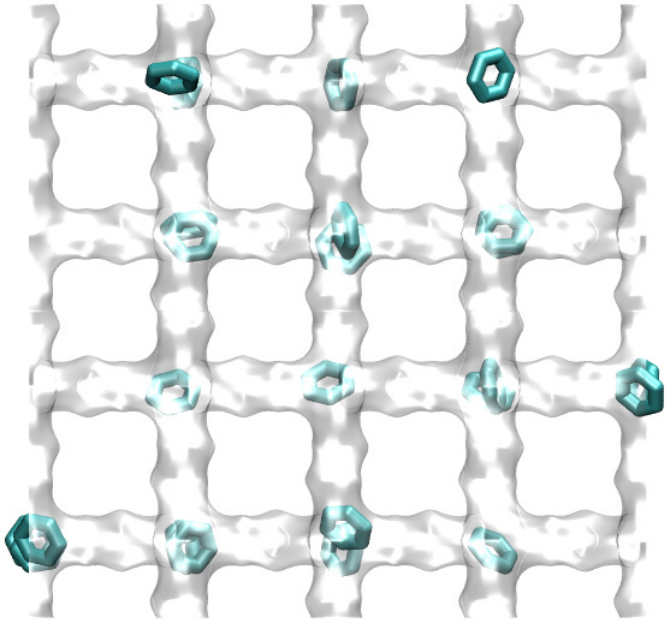

Figure 12

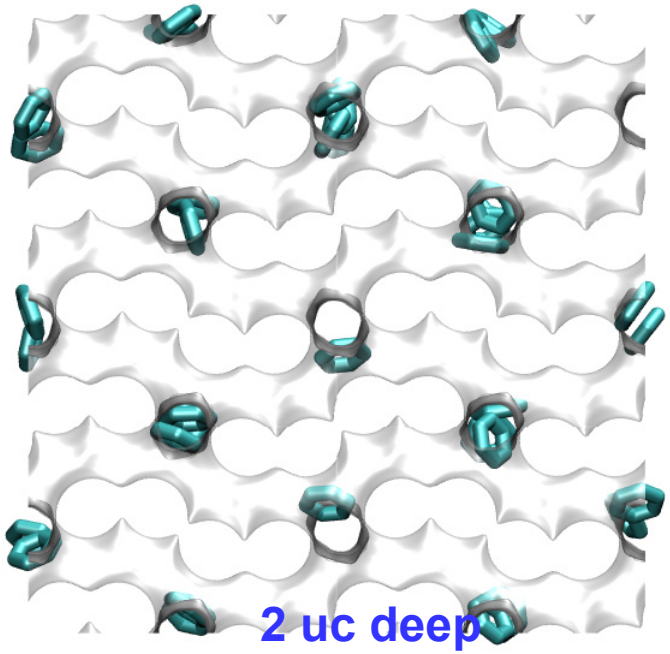

Benzene: 3 molecules/uc

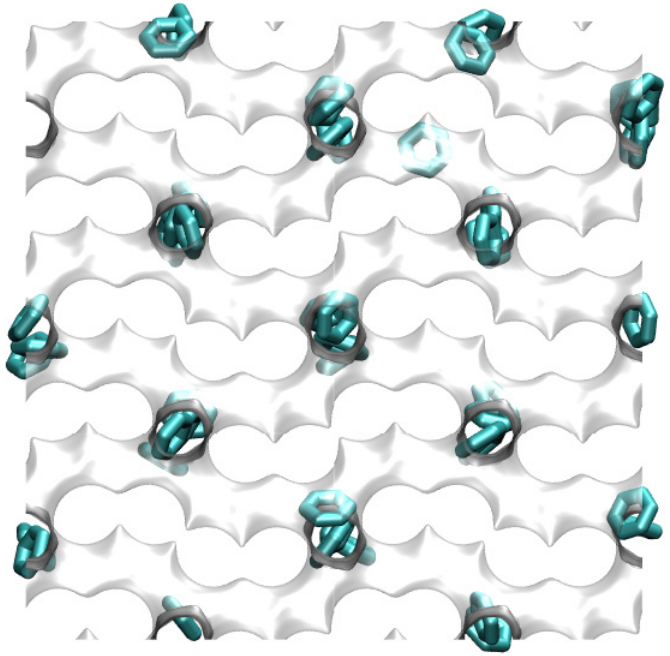

Benzene: 4 molecules/uc

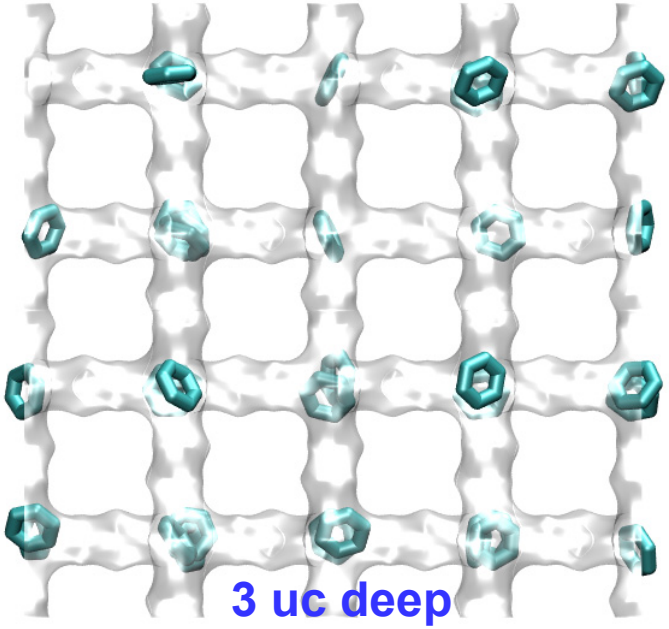

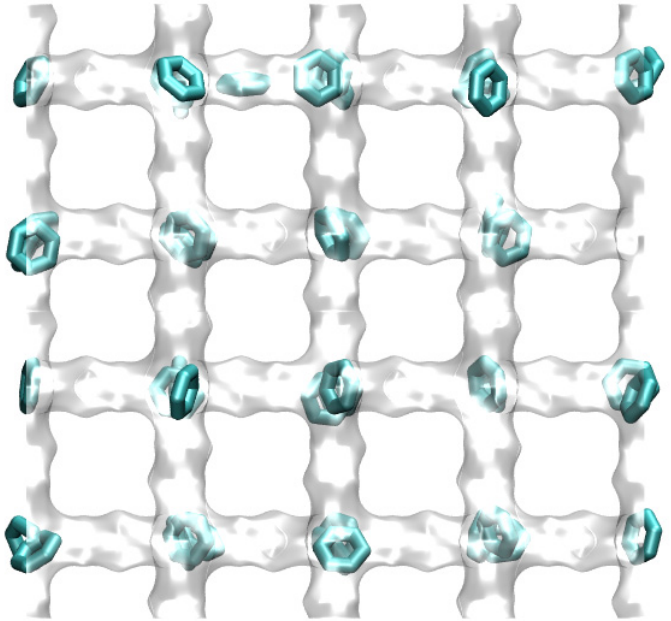

Figure 13

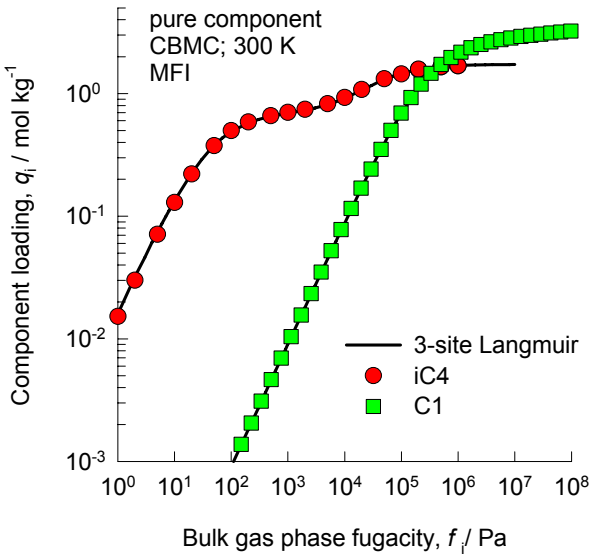

Pure components adsorption

C1 - iC4 / MFI / 300K

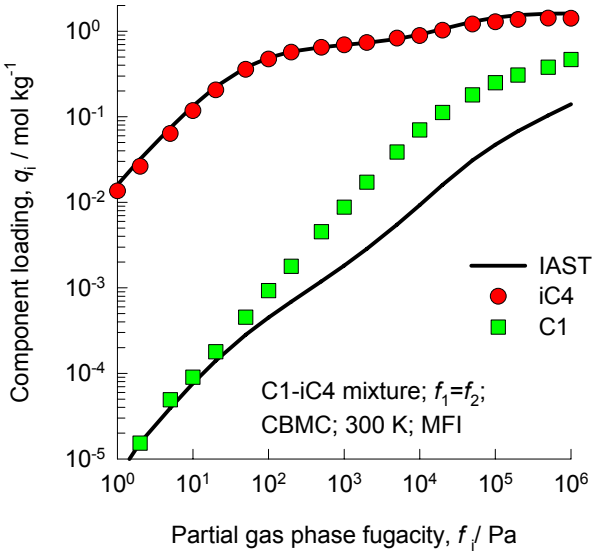

mixture adsorption

Figure 14

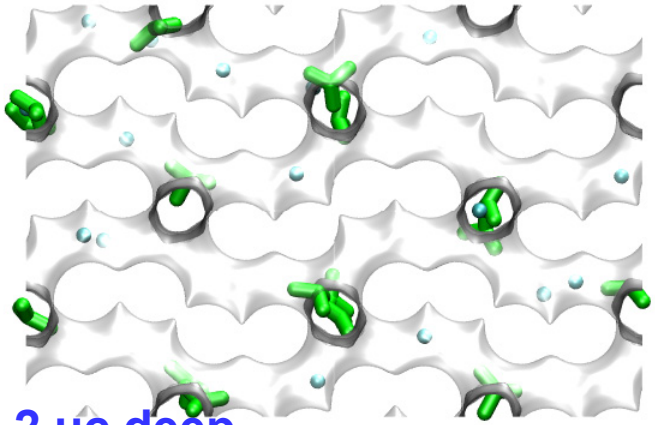

2 uc deep

C1 = 2 molecules/uc
iC4 = 2 molecules/uc

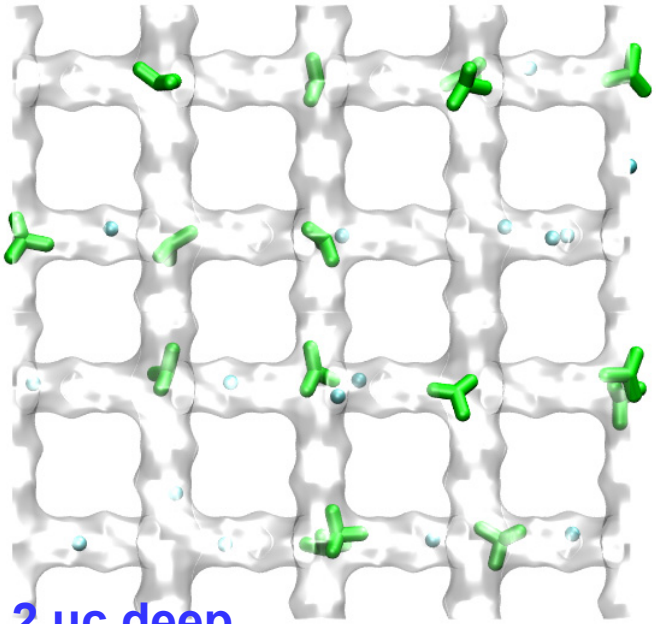

2 uc deep

C1 - iC4 / MFI / 300K

mixture diffusion

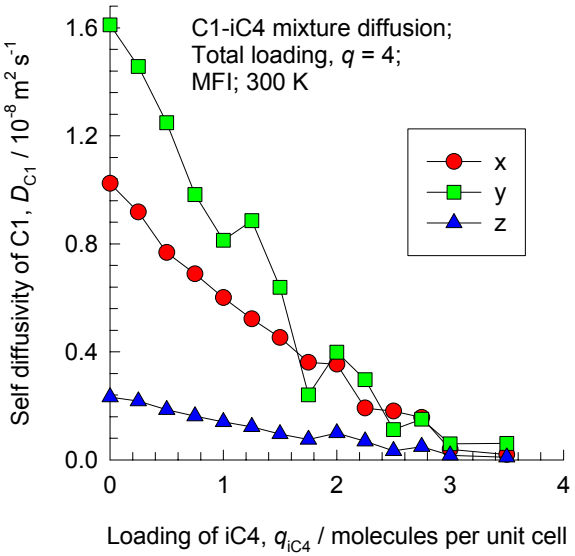

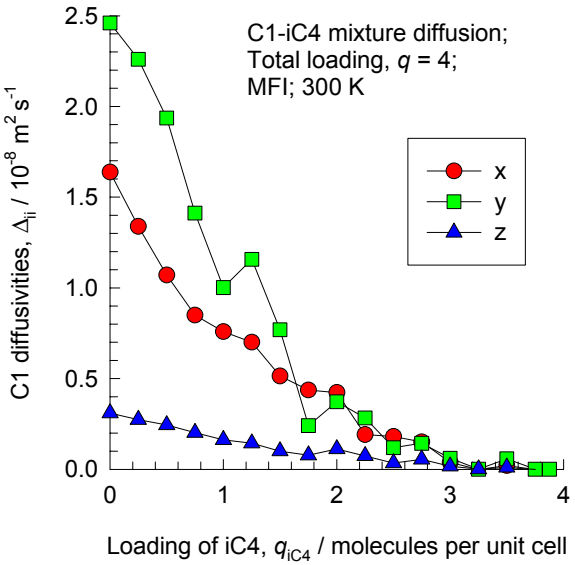

Figure 15

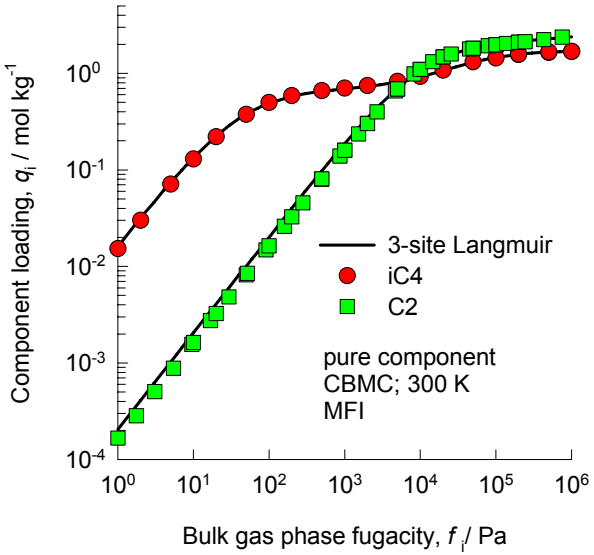

Pure components adsorption

C2 - iC4 / MFI / 300K

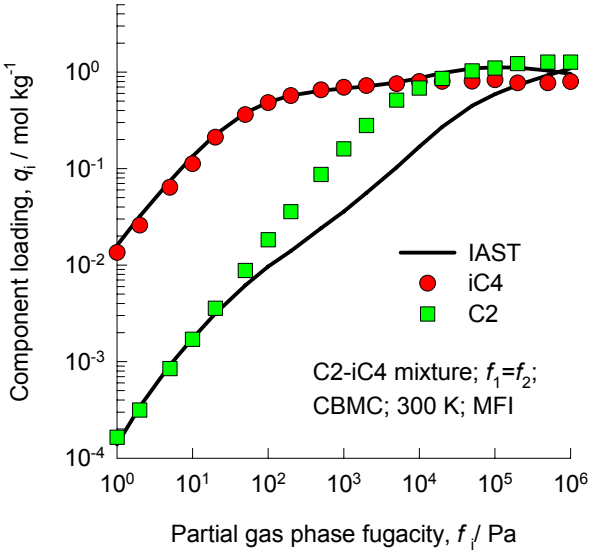

mixture adsorption

Figure 16

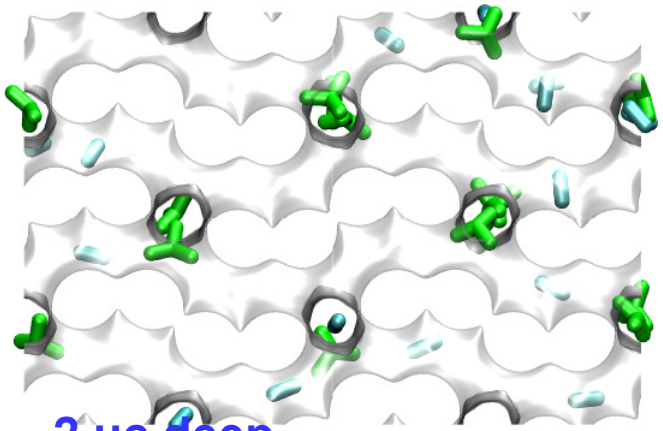

C2 = 2 molecules/uc
iC4 = 2 molecules/uc

C2 - iC4 / MFI / 300K

mixture diffusion

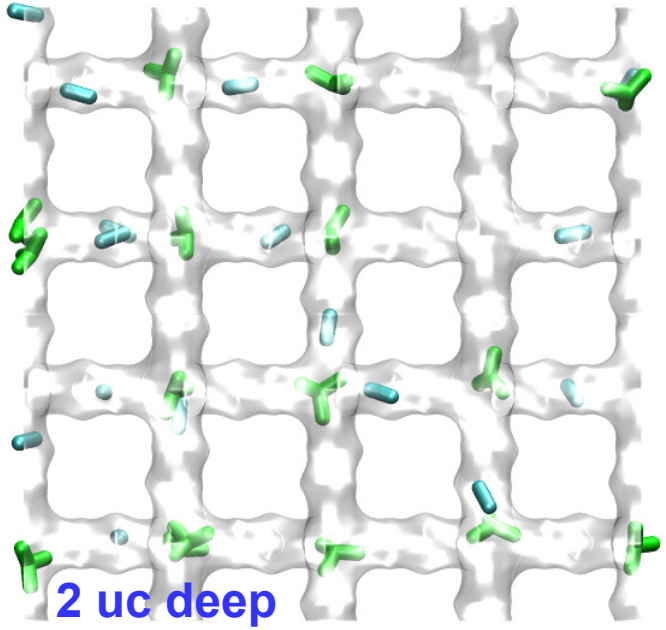

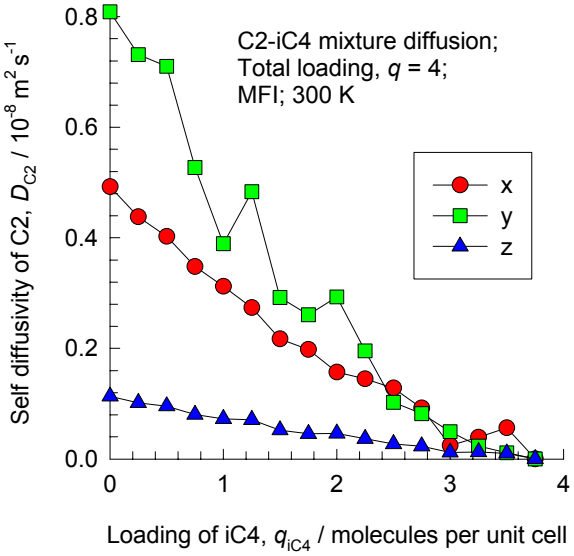

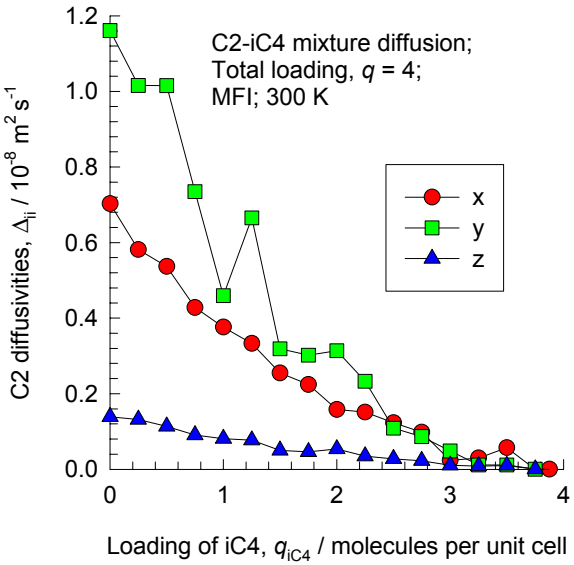

Figure 17

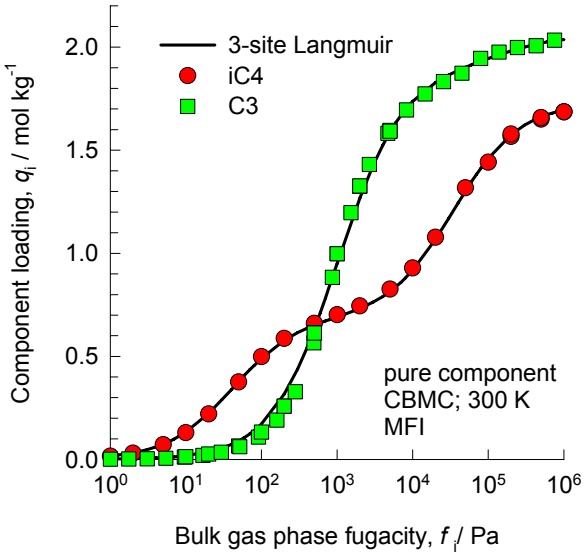

Pure components adsorption

C3 - iC4 / MFI / 300K

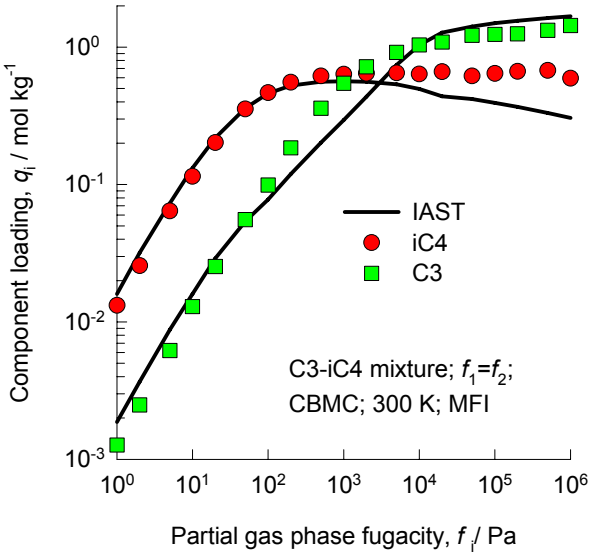

mixture adsorption

Figure 18

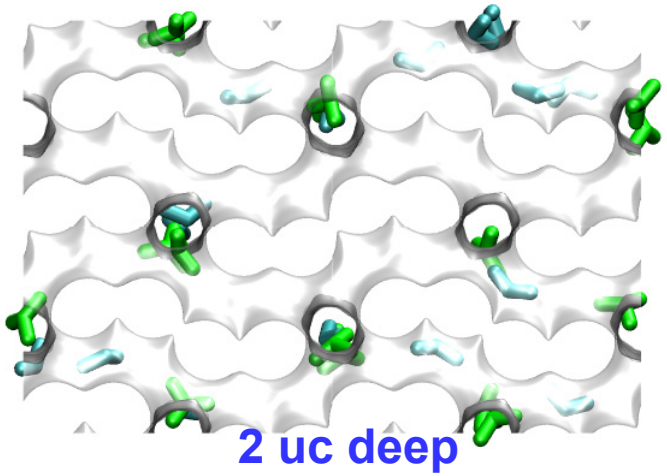

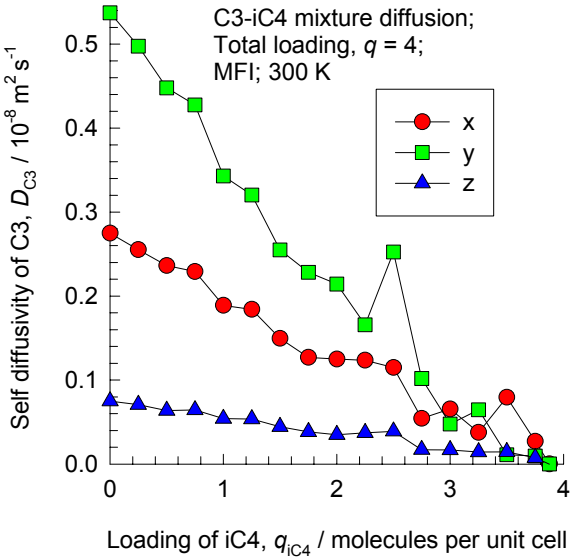

C3 = 2 molecules/uc
iC4 = 2 molecules/uc

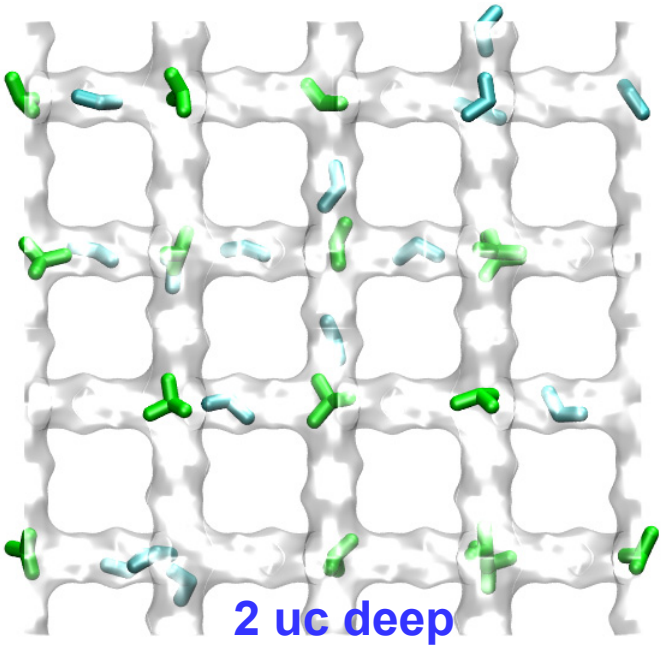

C3 - iC4 / MFI / 300K

mixture diffusion

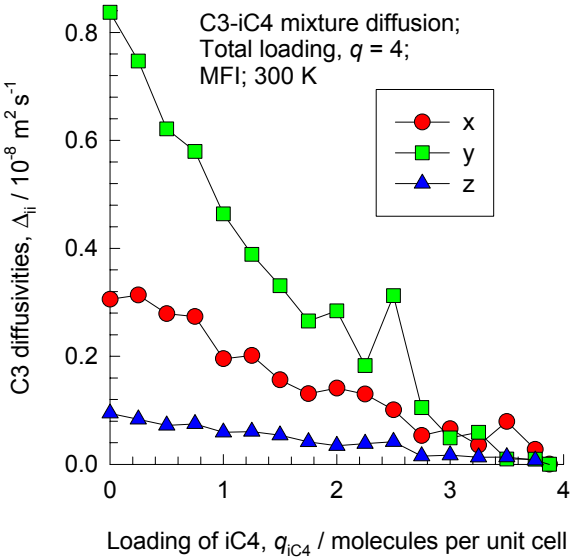

Figure 19

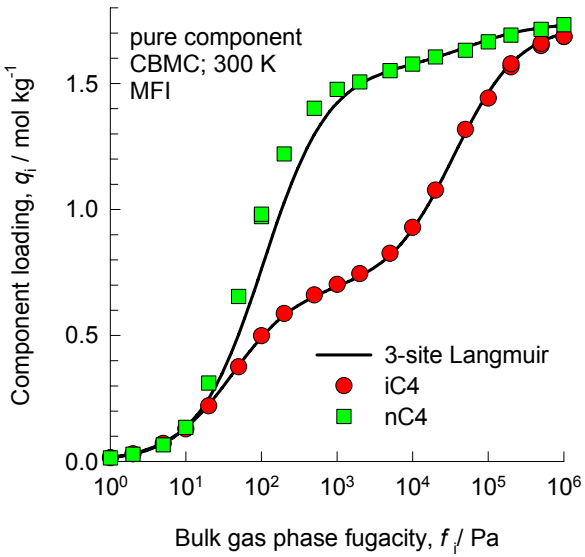

Pure components adsorption

nC4 - iC4 / MFI / 300K

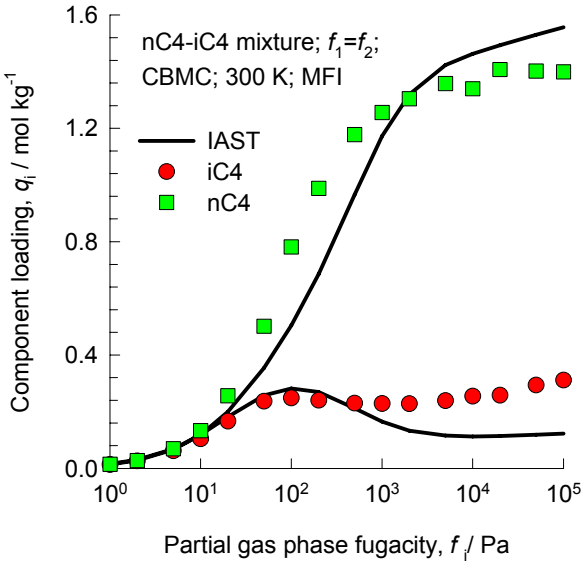

mixture adsorption

Figure 20

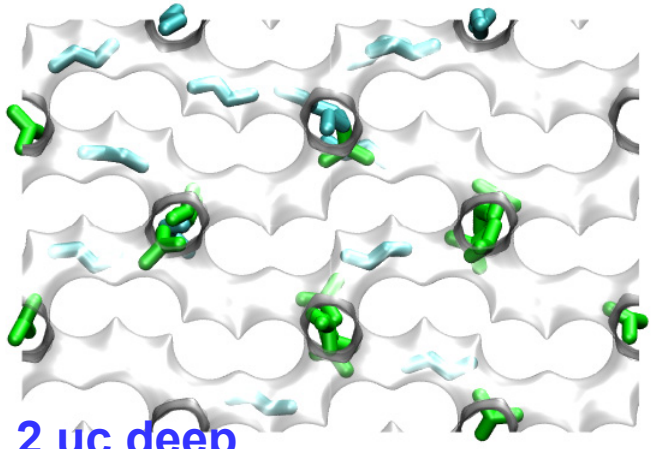

2 uc deep

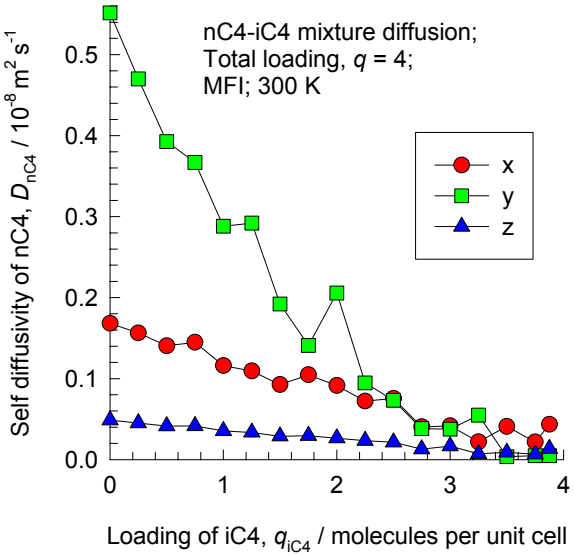

nC4 = 2 molecules/uc
iC4 = 2 molecules/uc

nC4 - iC4 / MFI / 300K

mixture diffusion

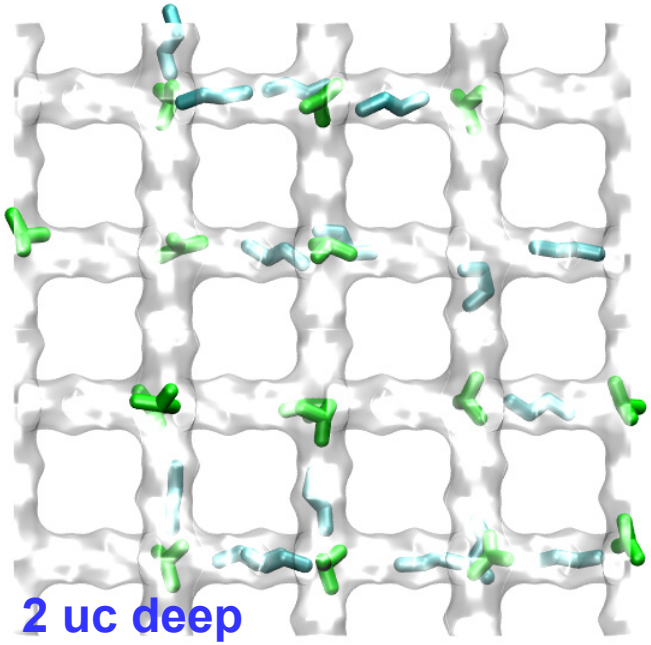

2 uc deep

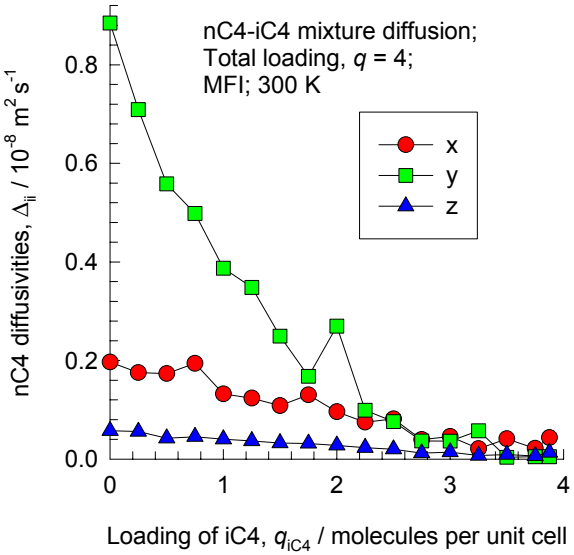

Figure 21

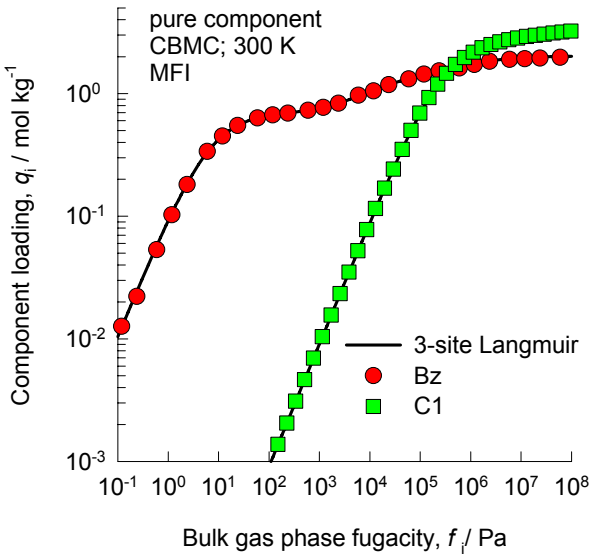

Pure components adsorption

C1 - Benzene/ MFI / 300K

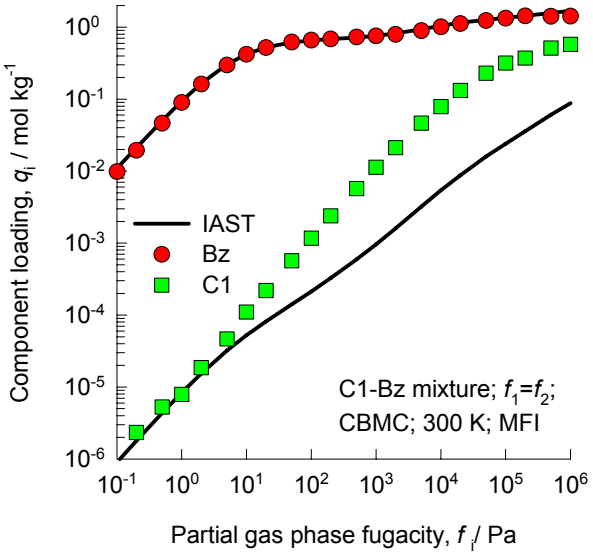

mixture adsorption

Figure 22

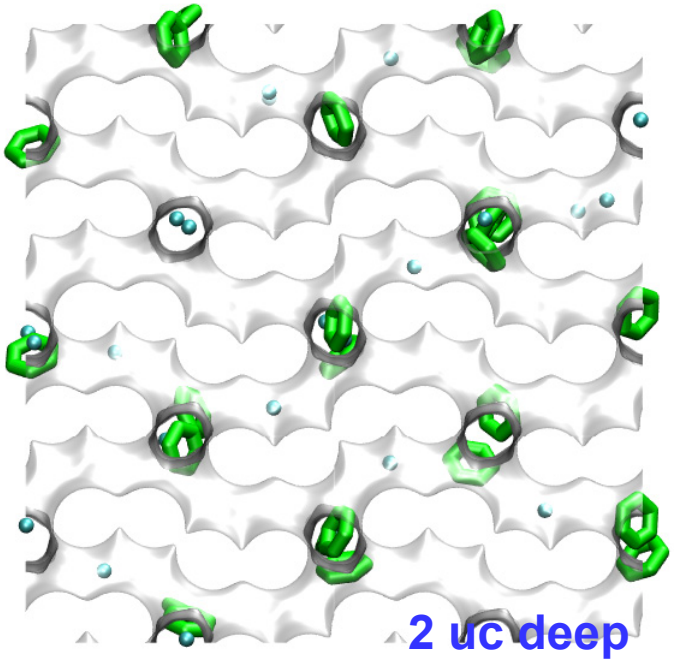

C1 = 2 molecules/uc
Benzene = 2 molecules/uc

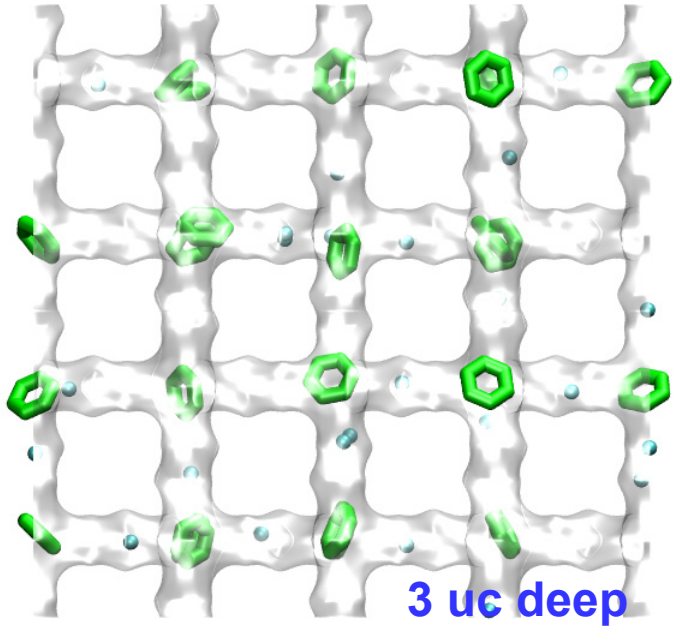

C1 - Benzene / MFI / 300K

mixture diffusion

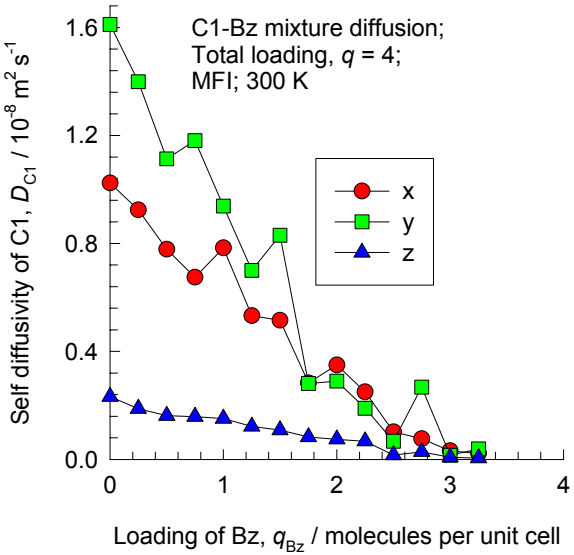

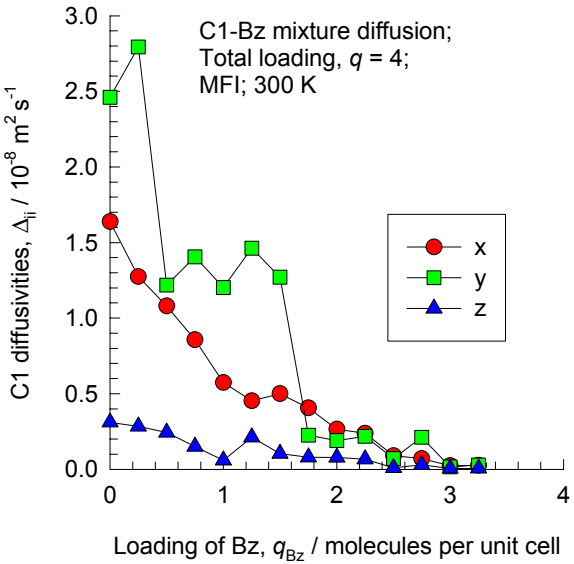

Figure 23

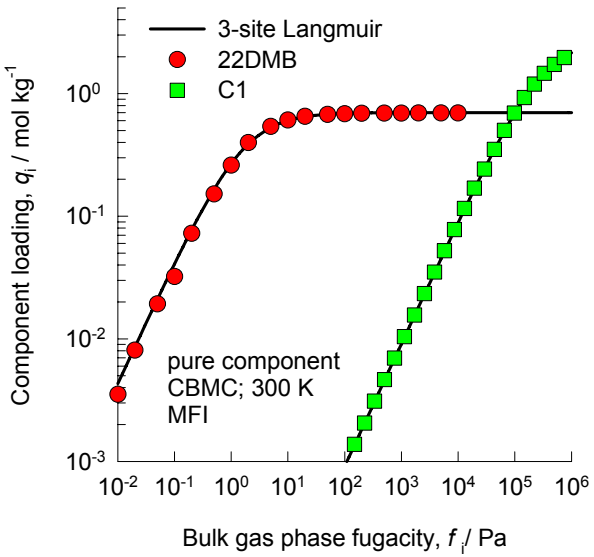

Pure components adsorption

C1 - 22DMB/ MFI / 300K

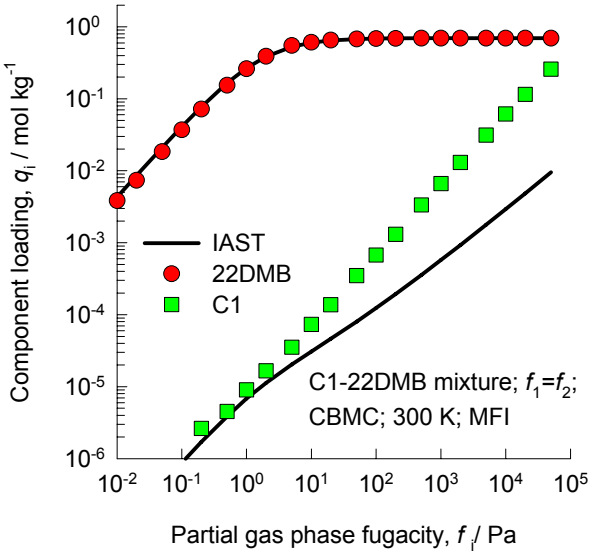

mixture adsorption

Figure 24

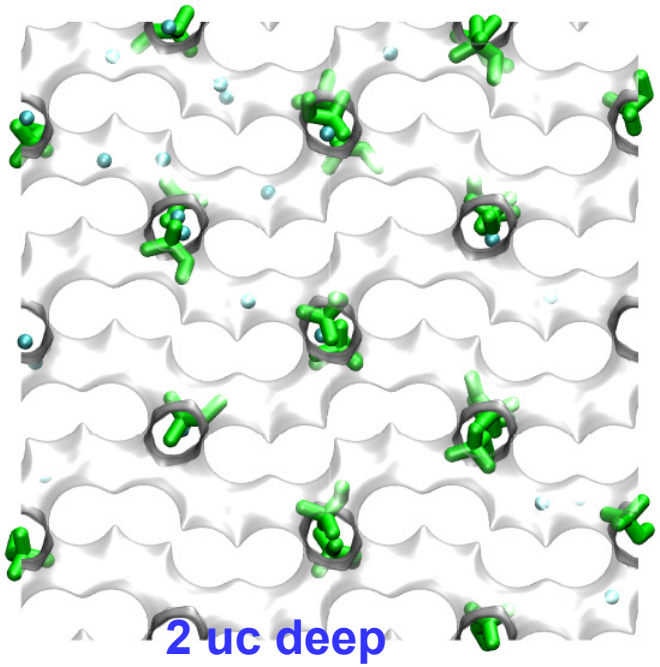

2 uc deep

C1 = 2 molecules/uc

22DMB = 2 molecules/uc

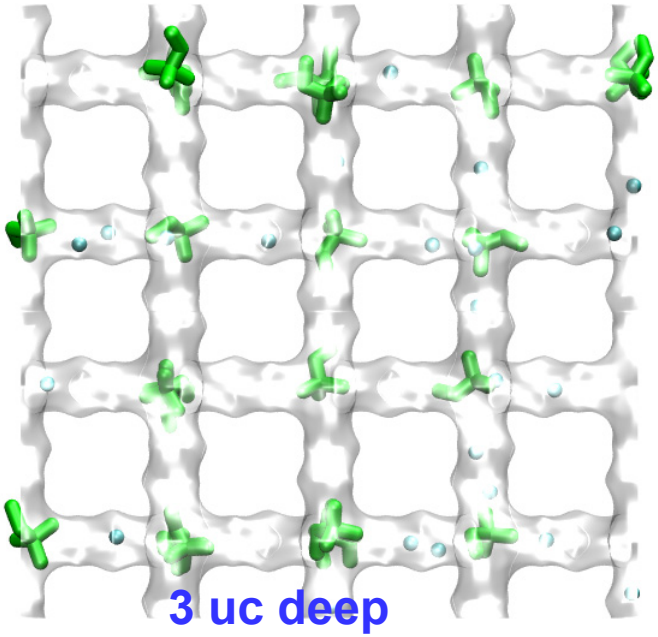

3 uc deep

C1 - 22DMB / MFI / 300K

mixture diffusion

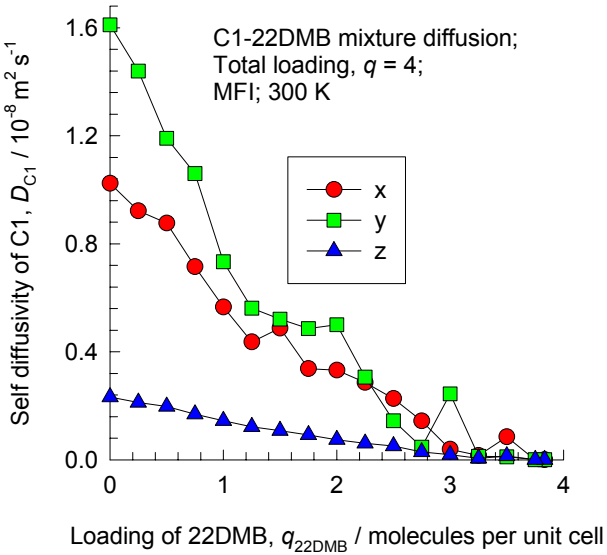

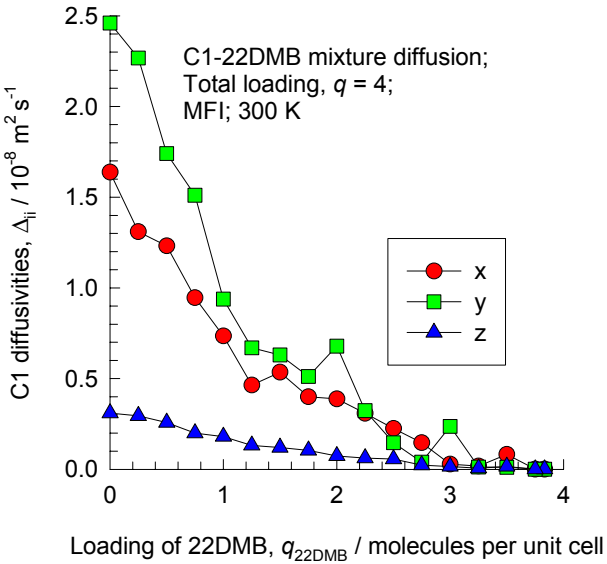

Figure 25

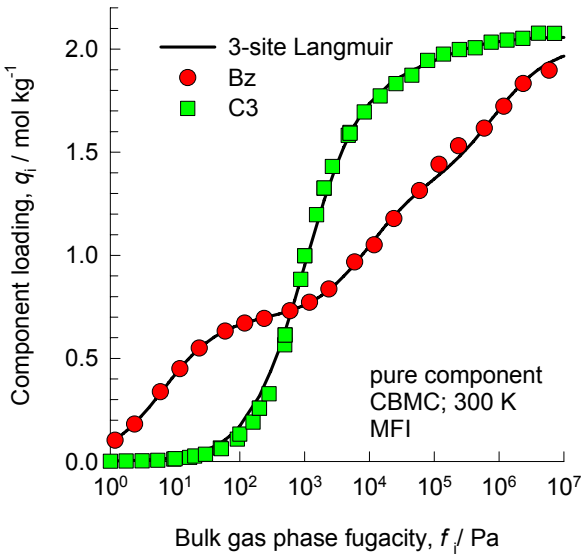

Pure components adsorption

C3 - Benzene/ MFI / 300K

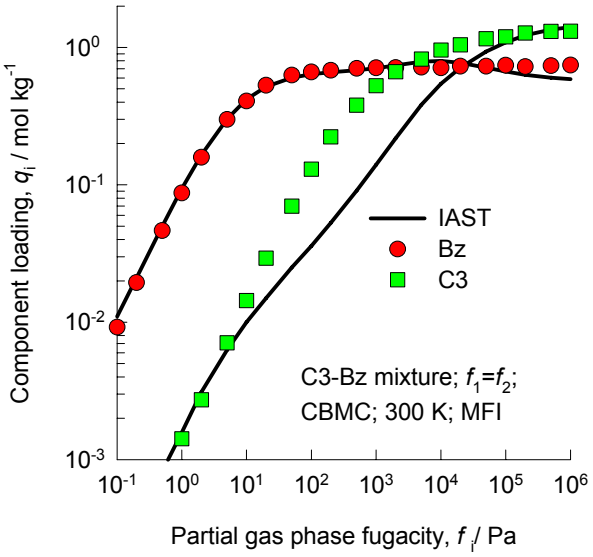

mixture adsorption

Figure 26

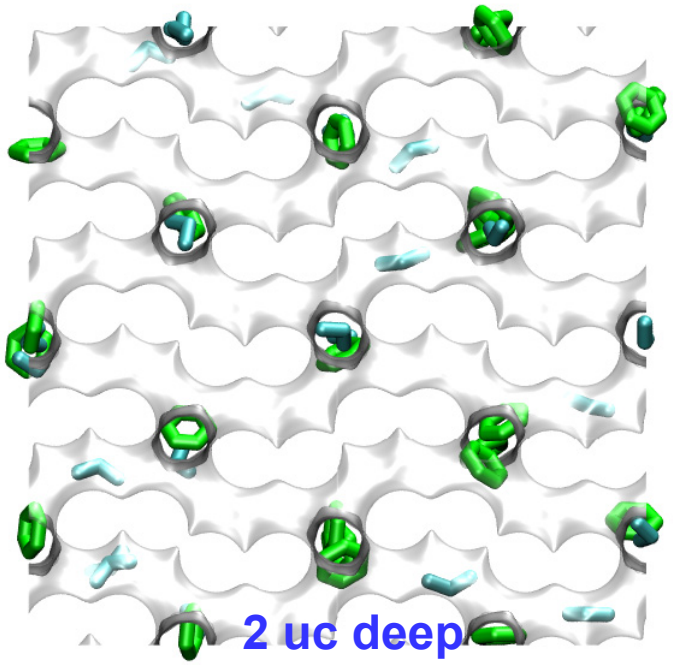

C3 = 2 molecules/uc
Benzene = 2 molecules/uc

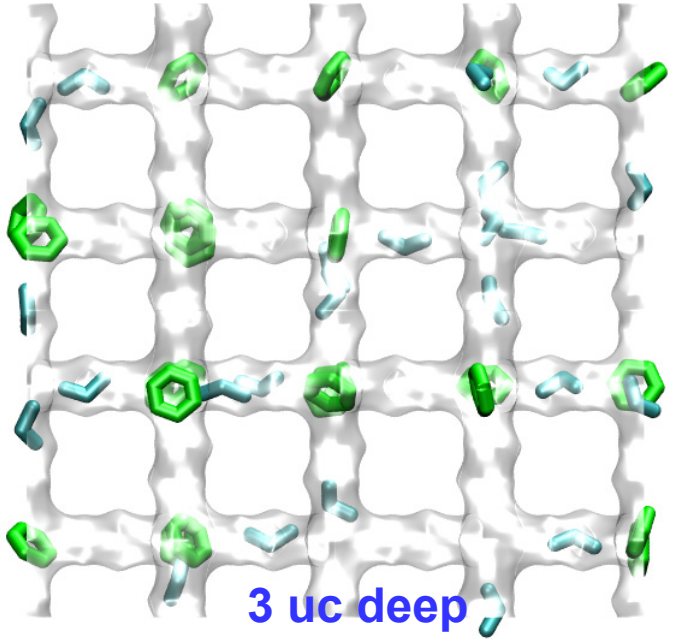

C3 - Benzene / MFI / 300K

mixture diffusion

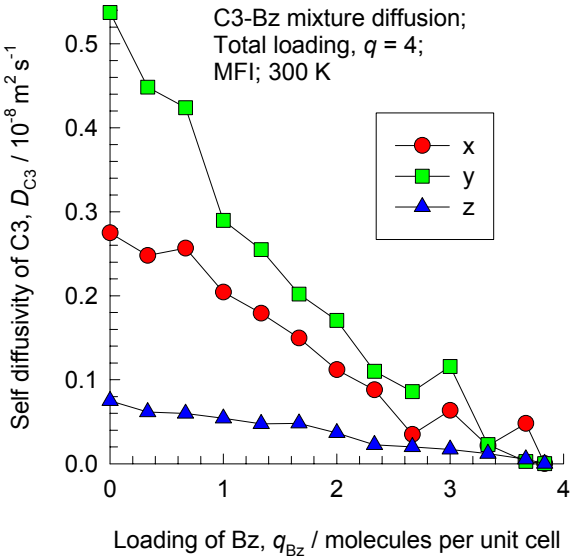

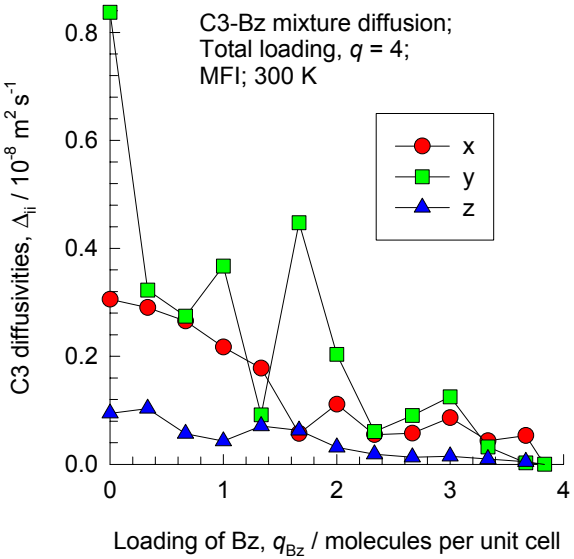

Figure 27

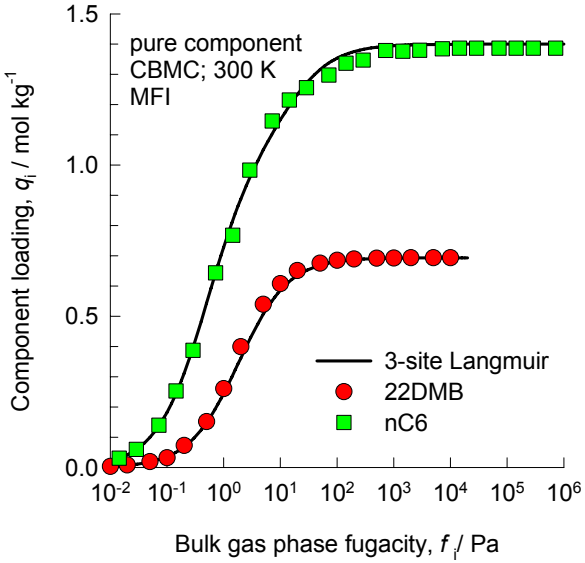

Pure components adsorption

nC6 -22DMB/ MFI / 300K

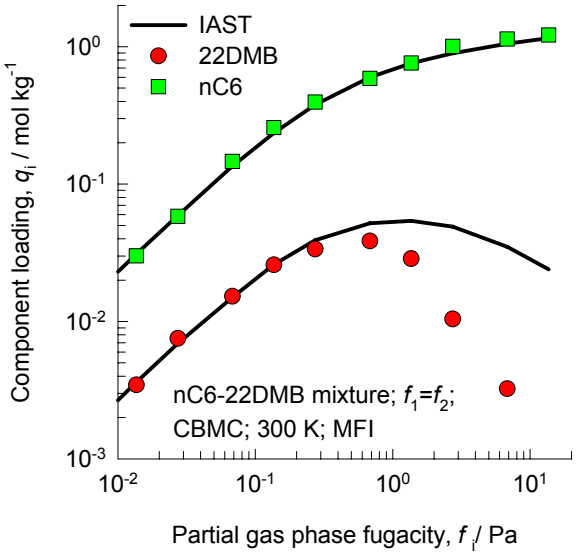

mixture adsorption

Figure 28

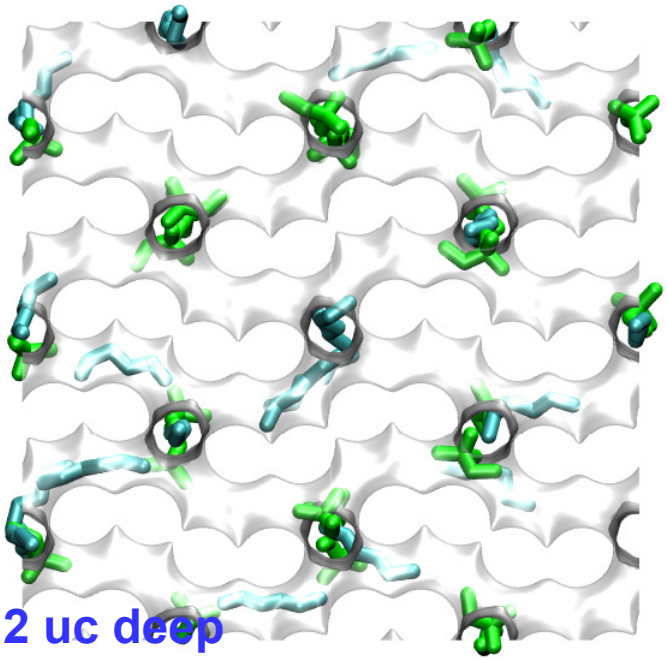

2 uc deep
nC6 = 2 molecules/uc
22DMB = 2 molecules/uc

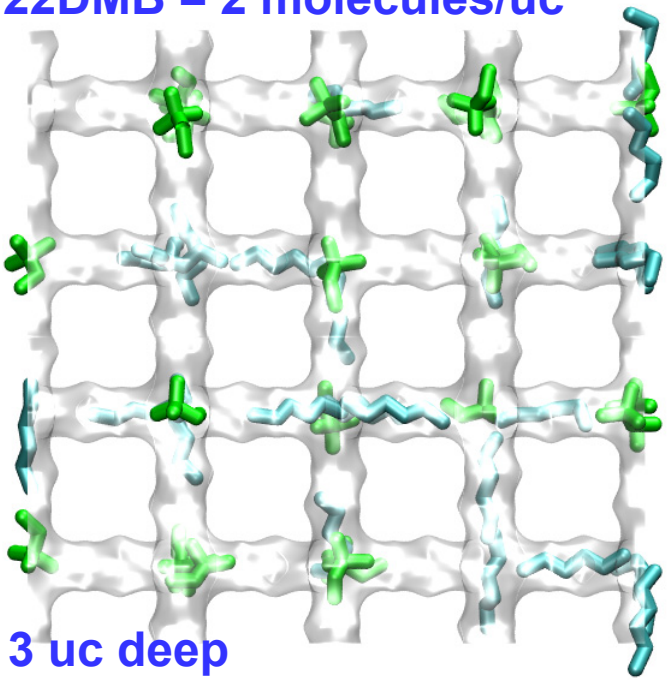

3 uc deep

nC6 - 22DMB / MFI / 300K

mixture diffusion

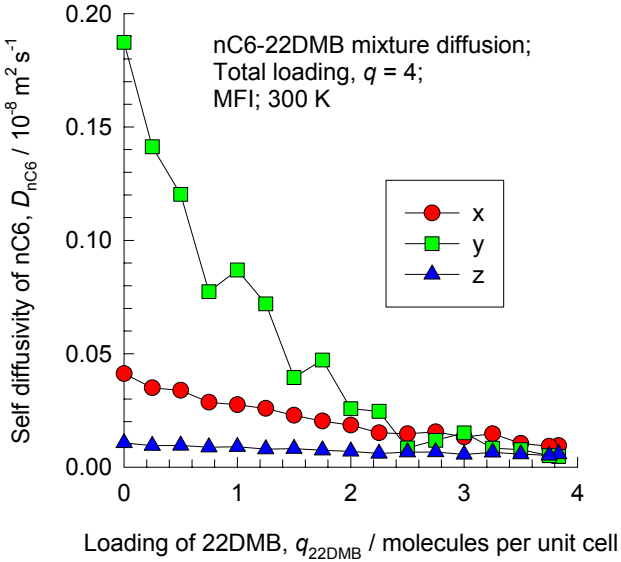

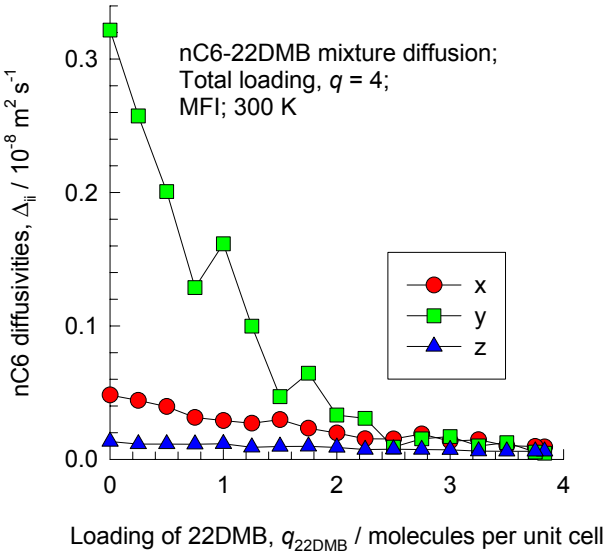

Figure 29

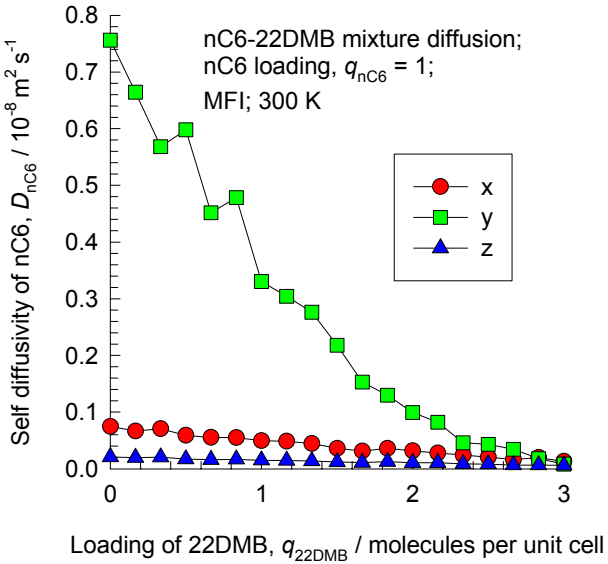

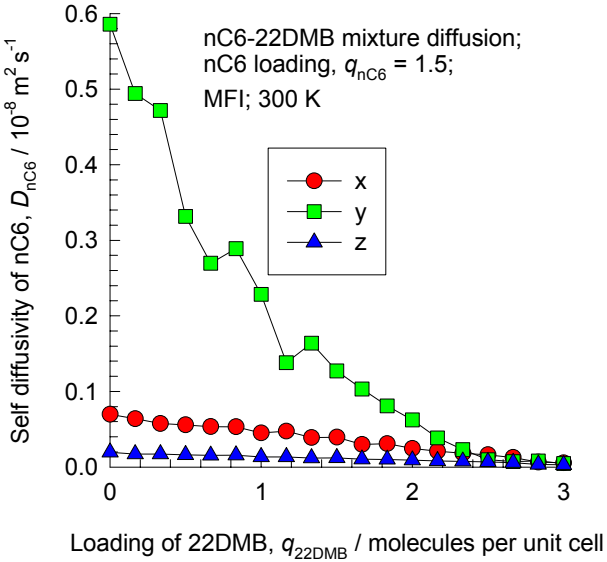

mixture diffusion

nC6 - 22DMB / MFI / 300K

mixture diffusion

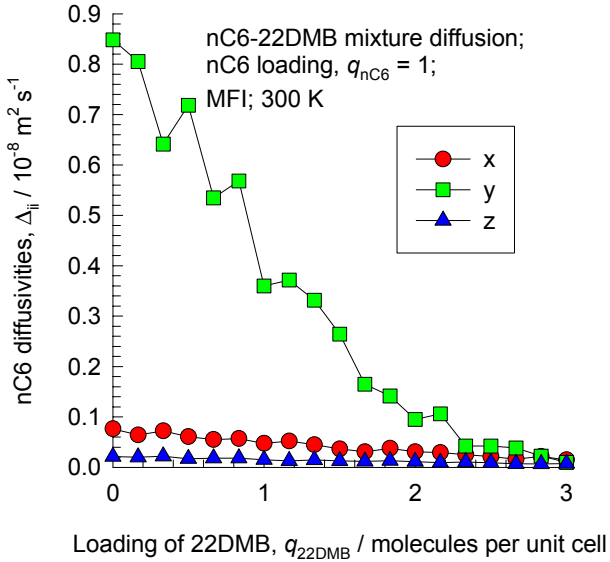

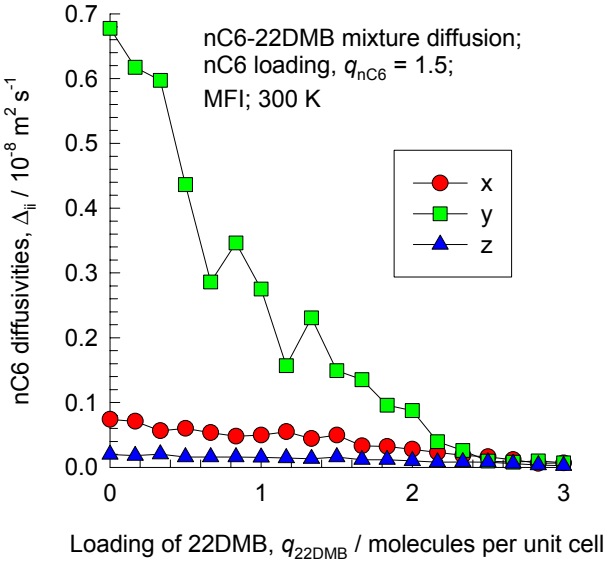

Figure 30

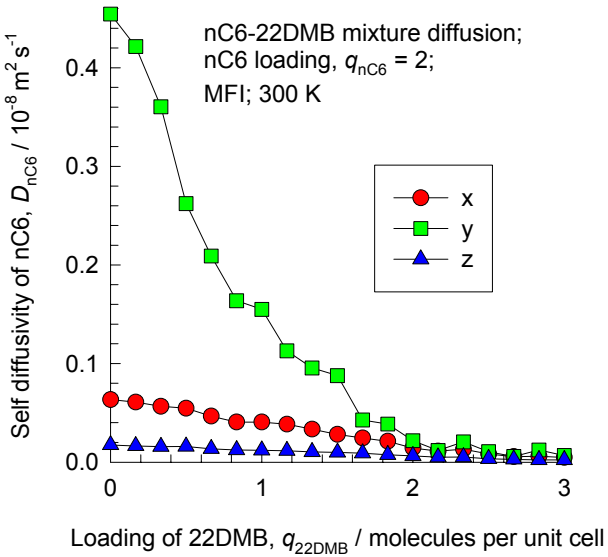

mixture diffusion

nC6 - 22DMB / MFI / 300K

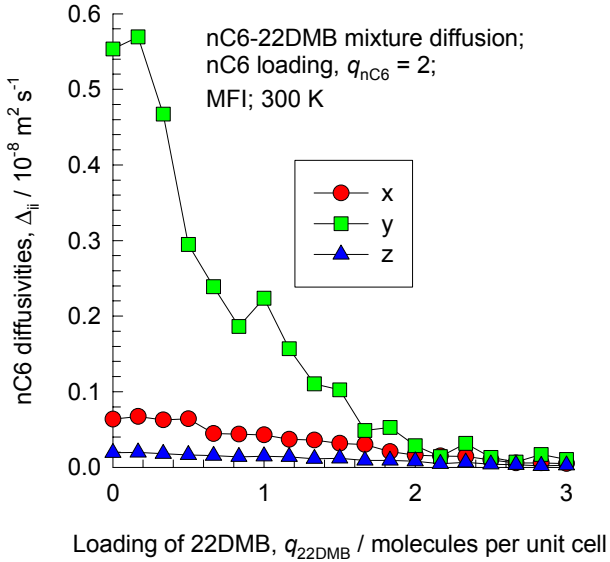

Figure 31

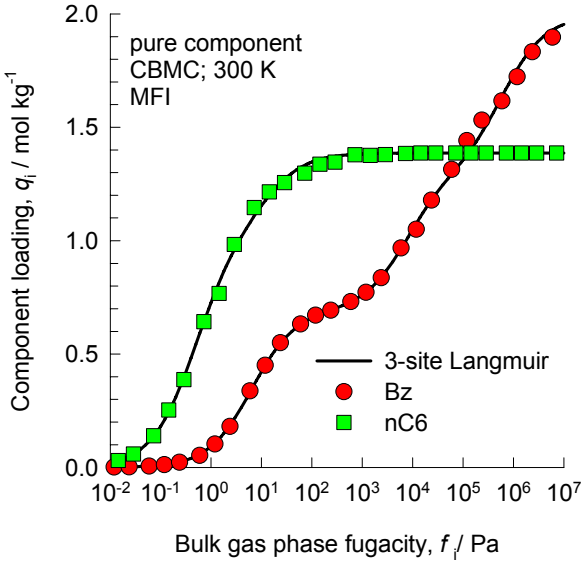

Pure components adsorption

nC6 -Bz/ MFI / 300K

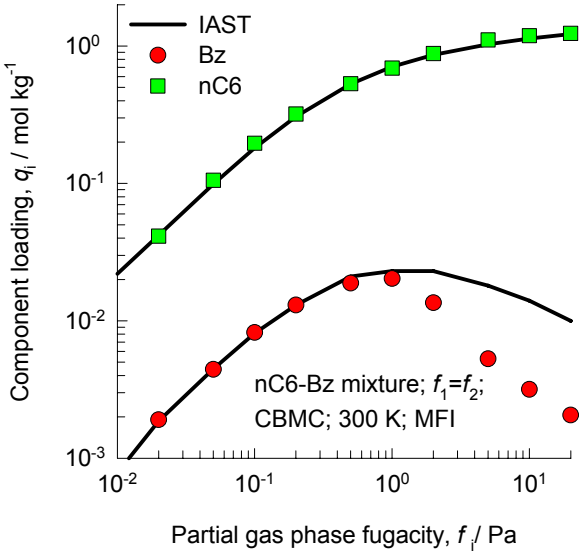

mixture adsorption

Figure 32

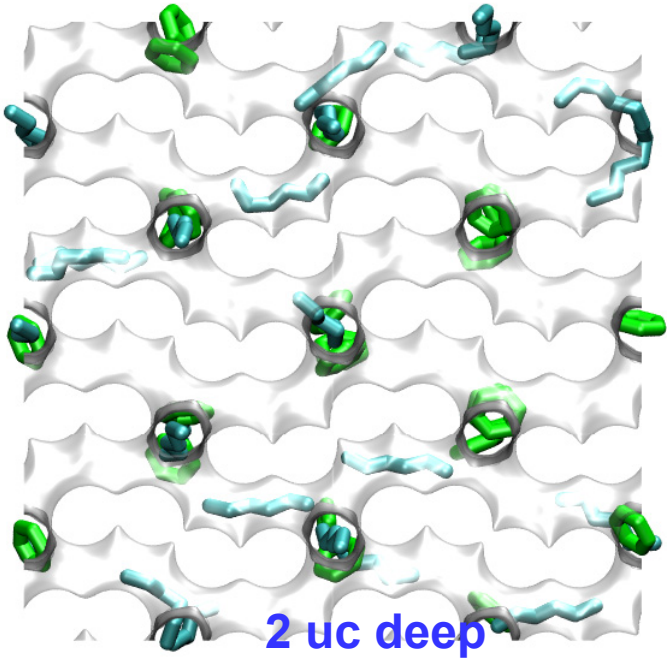

nC6 -Bz/ MFI / 300K

mixture diffusion

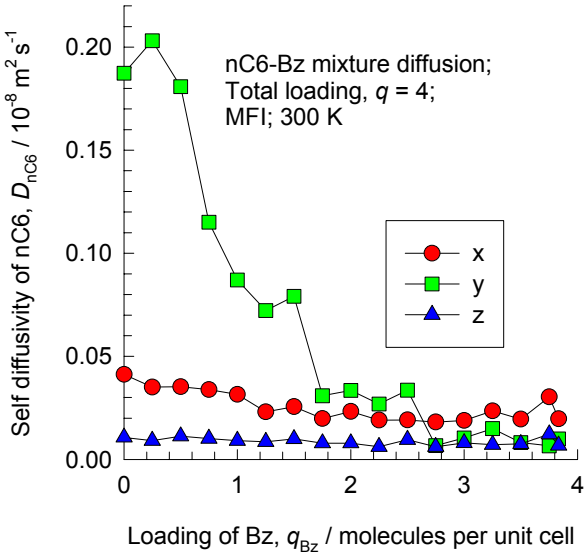

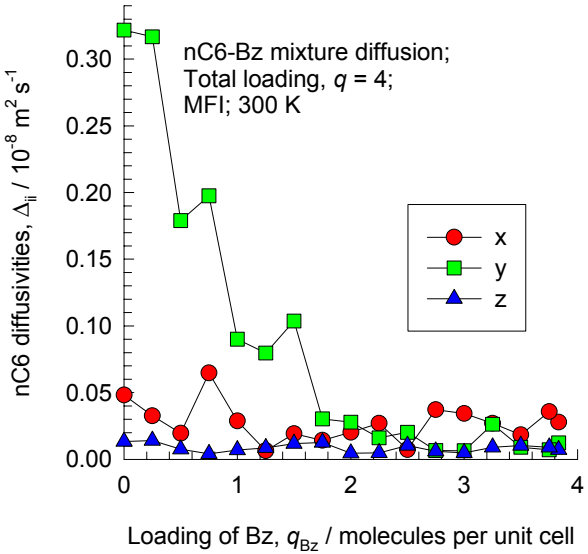

Figure 33

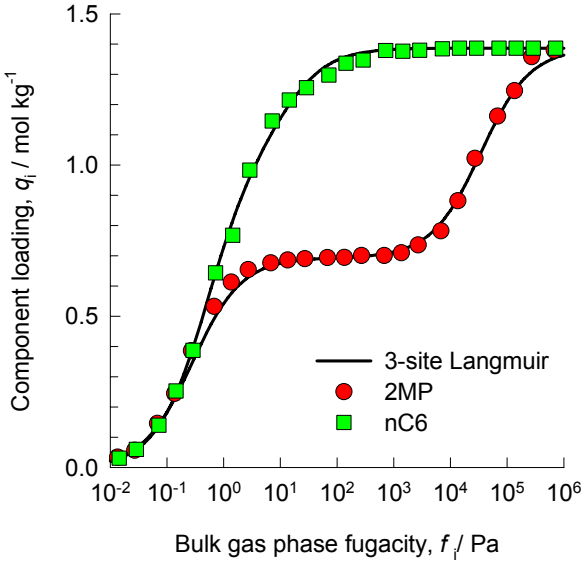

Pure components adsorption

nC6 -2MP/ MFI / 300K

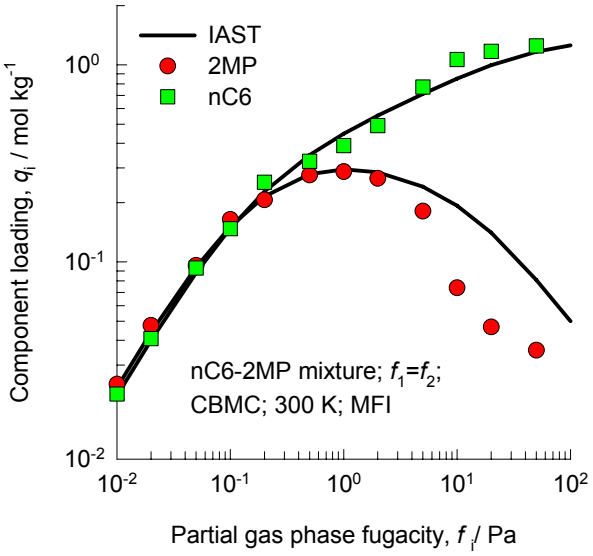

mixture adsorption

Figure 34

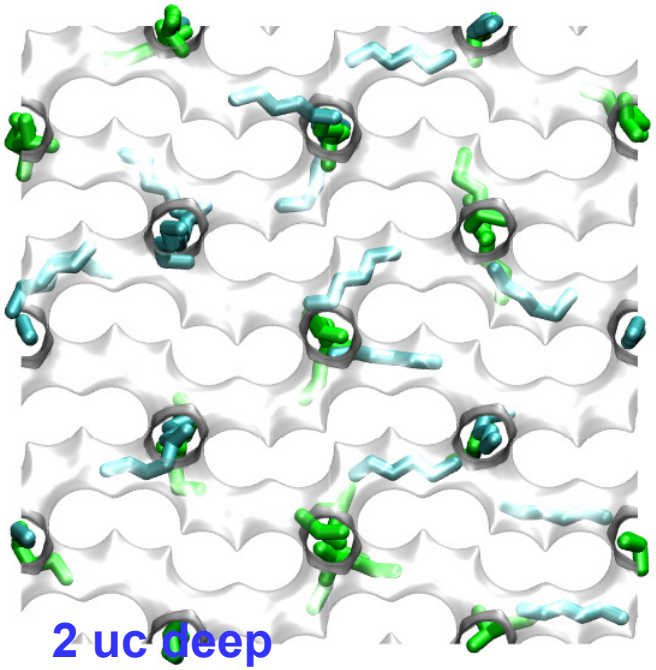

nC6 = 2 molecules/uc

2MP = 2 molecules/uc

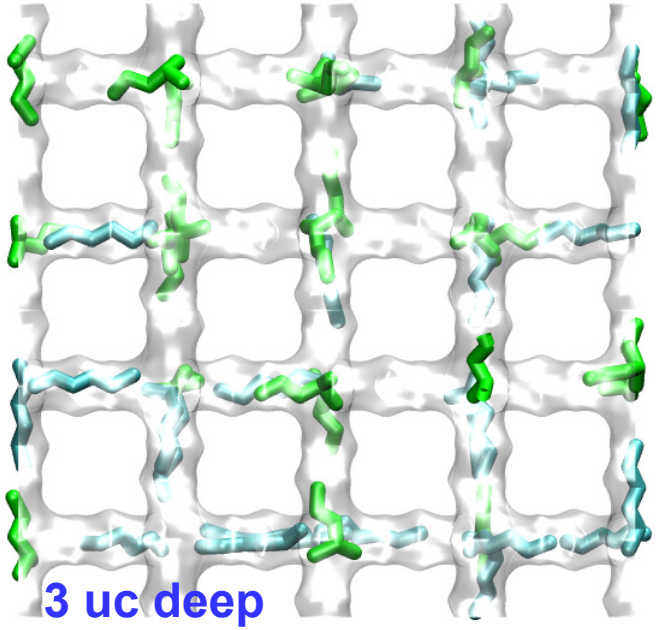

nC6 – 2MP/ MFI

mixture diffusion

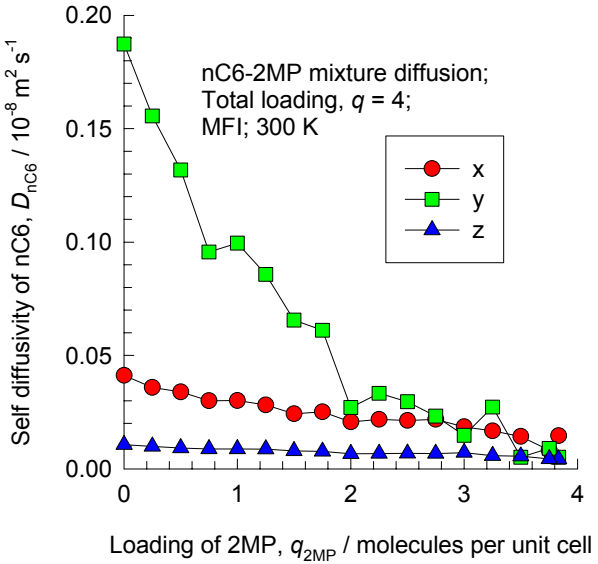

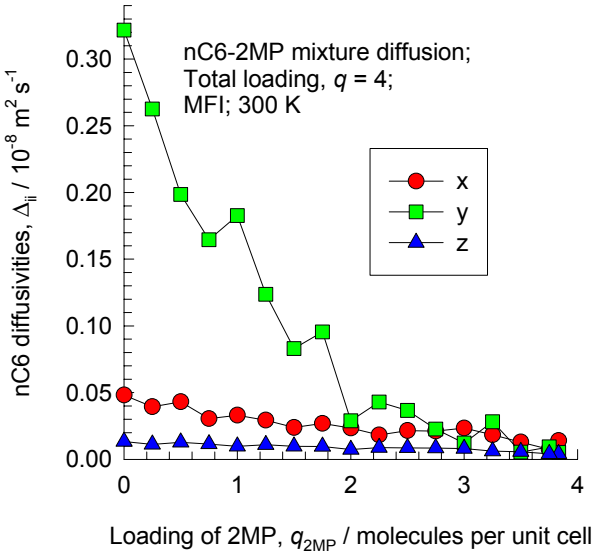

Figure 35

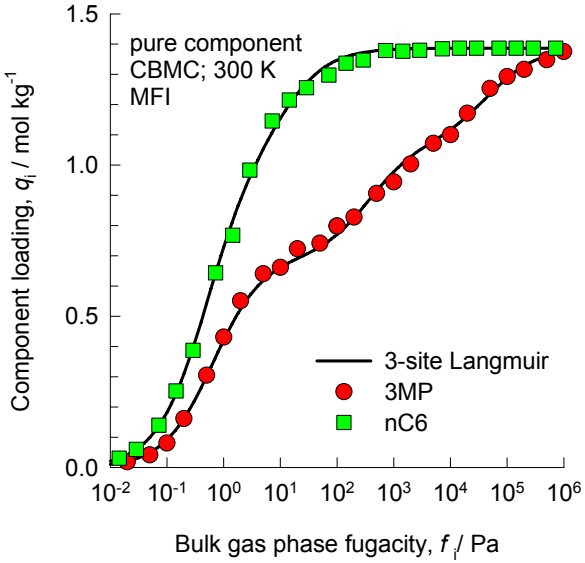

Pure components adsorption

nC6 -3MP/ MFI / 300K

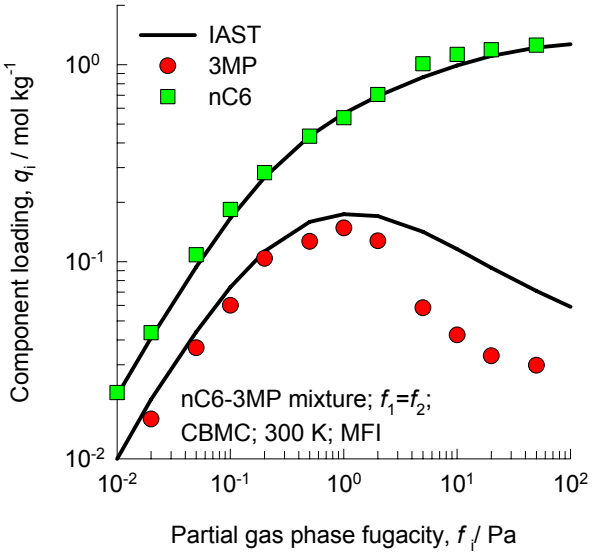

mixture adsorption

Figure 36

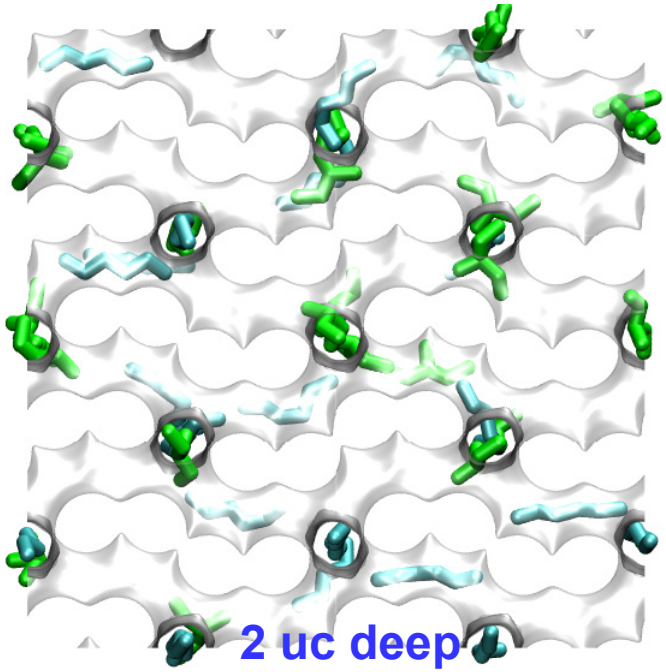

nC6 -3MP/ MFI / 300K

mixture diffusion